Astronomy & Astrophysics

Determination of the mass of the neutron star in SMC X−1, LMC X−4, and Cen X−3 with VLT/UVES[⋆,⋆⋆,⋆⋆⋆]

A. van der Meer[1], L. Kaper[1,2], M. H. van Kerkwijk[3], M. H. M. Heemskerk[1], and E. P. J. van den Heuvel[1,2]

[1] Astronomical Institute "Anton Pannekoek", University of Amsterdam, Kruislaan 403, 1098 SJ Amsterdam, The Netherlands
e-mail: ameer@science.uva.nl
[2] Center for High-Energy Astrophysics, Kruislaan 403, 1098 SJ, The Netherlands
[3] Department of Astronomy and Astrophysics, University of Toronto, 60 St George Street, Toronto, ON M5S 3H8, Canada

ABSTRACT

We present the results of a spectroscopic monitoring campaign of the OB-star companions to the eclipsing X-ray pulsars SMC X−1, LMC X−4 and Cen X−3. High-resolution optical spectra obtained with UVES on the ESO *Very Large Telescope* are used to determine the radial-velocity orbit of the OB (super)giants with high precision. The excellent quality of the spectra provides the opportunity to measure the radial-velocity curve based on individual lines, and to study the effect of possible distortions of the line profiles due to e.g. X-ray heating on the derived radial-velocity amplitude. Several spectral lines show intrinsic variations with orbital phase. The magnitude of these variations depends on line strength, and thus provides a criterion to select lines that do not suffer from distortions. The undistorted lines show a larger radial-velocity amplitude than the distorted lines, consistent with model predictions. Application of our line-selection criteria results in a mean radial-velocity amplitude K_{opt} of 20.2 ± 1.1, 35.1 ± 1.5, and 27.5 ± 2.3 km s^{-1} (1σ errors), for the OB companion to SMC X−1, LMC X−4 and Cen X−3, respectively. Adding information on the projected rotational velocity of the OB companion (derived from our spectra), the duration of X-ray eclipse and orbital parameters of the X-ray pulsar (obtained from literature), we arrive at a neutron star mass of $1.06^{+0.11}_{-0.10}$, $1.25^{+0.11}_{-0.10}$ and $1.34^{+0.16}_{-0.14}$ $M_{\odot}$ for SMC X−1, LMC X−4 and Cen X−3, respectively. The mass of SMC X−1 is near the minimum mass (∼1 $M_{\odot}$) expected for a neutron star produced in a supernova. We discuss the implications of the measured mass distribution on the neutron-star formation mechanism, in relation to the evolutionary history of the massive binaries.

Key words. stars: binaries: eclipsing – stars: neutron – stars: general – equation of state – accretion, accretion disks

1. Introduction

A neutron star is the compact remnant of a massive star ($M \gtrsim 8\ M_{\odot}$) with a central density that can be as high as 5 to 10 times the density of an atomic nucleus. The global structure of a neutron star depends on the equation of state (EOS) under these extreme conditions, i.e. the relation between pressure and density in the neutron star interior (e.g. Lattimer & Prakash 2004). Given an EOS, a mass-radius relation for the neutron star and a corresponding maximum neutron-star mass can be derived. The "stiffness" of the EOS depends e.g. on how many bosons are present in matter of such a high density. As bosons do not contribute to the fermi pressure, their presence will tend to "soften" the EOS. For a soft EOS, the maximum neutron-star mass will be low (e.g. <1.55 $M_{\odot}$ for the EOS applied by Brown & Bethe 1994); for a higher mass, the object would collapse into a black hole.

The accurate measurement of neutron-star masses is therefore important for our understanding of the EOS of matter at supra-nuclear densities. Currently, the most massive neutron star in an X-ray binary is the X-ray pulsar Vela X−1

(Barziv et al. 2001; Quaintrell et al. 2003) with a mass of $1.86 \pm 0.16\ M_{\odot}$. The millisecond radio pulsar J0751+1807 likely has an even higher mass: $2.1 \pm 0.2\ M_{\odot}$ (Nice et al. 2005). Both results are in favor of a stiff EOS (see also Srinivasan 2001). Neutron stars also have a minimum mass limit. The minimum stable neutron-star mass is about $0.1\ M_{\odot}$, although a more realistic minimum stems from a neutron star's origin in a supernova. Lepton-rich proto neutron stars are unbound if their masses are less than about 1 $M_{\odot}$ (Lattimer & Prakash 2004; Haensel et al. 2002).

Another issue is the neutron-star mass distribution: the detailed supernova mass ejection mechanism accompanying the formation of the neutron star is not understood, but it is likely that the many neutrinos that are produced during the formation of the (proto-) neutron star in the centre of the collapsing star play an important role (e.g. Burrows 2000). Timmes et al. (1996) present model calculations from which they conclude that type II supernovae (massive, single stars) will give a bimodal neutron-star mass distribution, with peaks at 1.28 and 1.73 $M_{\odot}$, while type Ib supernovae (such as produced by stars in binaries, which are stripped of their envelopes) will produce neutron stars within a small range around 1.32 $M_{\odot}$. Despite the fact that it is in a binary, the massive neutron star in Vela X−1 may belong to the second peak in this mass distribution.

Neutron stars are detected either as radio pulsars, single or in a binary with a white dwarf or neutron star companion, or as X-ray sources in binaries with a (normal) low-mass (LMXB) or a

---

Table 1. Orbital parameters of SMC X−1, LMC X−4 and Cen X−3 obtained from Wojdowski et al. (1998), Levine et al. (2000) and Nagase et al. (1992), respectively. T_0 is the mid-eclipse time and corresponds to orbital phase $\phi = 0.0$. The eccentricity is obtained from Bildsten et al. (1997) and references therein. All the reported errors are 1σ values unless stated otherwise. For SMC X−1 the range of semi-eclipse angle θ_e includes observations obtained by Primini et al. (1976), Bonnet-Bidaud & Van der Klis (1981) and Schreier et al. (1972a); for LMC X−4 those of Li et al. (1978), White (1978) and Pietsch et al. (1985); for Cen X−3 we list the result of Clark et al. (1988).

	SMC X−1	LMC X−4	Cen X−3
T_0 (MJD)	42836.18278(20)	51110.86579(10)	40958.35(1)
P_{orb} (days)	3.89229090(43)	1.40839776(26)	2.08713845(5)
$\dot{P}_{orb}/P_{orb}$ (yr^{-1})	$-3.353(14) \times 10^{-6}$	$-9.8(7) \times 10^{-7}$	$-1.738(4) \times 10^{-6}$
P_{spin} (s)	0.708	13.5	4.82
$a_X \sin i$ (lt-s)	53.4876(4)	26.343(16)	39.56(7)
e	$<4 \times 10^{-5}(2\sigma)$	0.006(2)	$<1.6 \times 10^{-3}(90\%)$
θ_e (deg)	26–30.5	25–29	32.9 ± 1.4
OB companion	B0 Ib	O8 III	O6.5 II-III

high-mass companion star (HMXB). Presently, all accurate mass determinations have been for neutron stars that were almost certainly formed in type Ib supernovae and that have accreted little since. Exceptions are J1909−3744, a pulsar (+ white dwarf) with a mass of $1.438 \pm 0.024\ M_\odot$ (Jacoby et al. 2005), and the massive neutron star in J0751+1807, which may have originated from an LMXB. The most accurate masses have been derived for the binary radio pulsars. Until recently, all of these were consistent with a small mass range near $1.35\ M_\odot$ (Thorsett & Chakrabarty 1999).

We focus here on the initially most massive systems, which consist of a massive OB supergiant and a neutron star or a black hole (Kaper 2001; Kaper & Van der Meer 2005). The main motivation to concentrate on these systems is that they are the most likely hosts of massive neutron stars. About a dozen of these systems are known[1]; five of them contain an eclipsing X-ray pulsar. The masses of all but one (Vela X−1) are consistent (within their errors) with a value of about $1.4\ M_\odot$. However, most spectroscopic observations used for these mass determinations were carried out more than 20 years ago, before the advent of sensitive CCD detectors and 8m-class telescopes, which allow high-resolution spectroscopy of the optical companions. The uncertainties in the earlier radial velocity measurements (see Van Kerkwijk et al. 1995a) are too large to measure a significant spread in mass among these neutron stars, if present.

In this paper we present new, more accurate determinations of the mass of the neutron star in three of these systems, i.e. SMC X−1, LMC X−4, and Cen X−3 using the high-resolution Ultraviolet and Visual Echelle Spectrograph (UVES) on the ESO *Very Large Telescope* (VLT). These systems are in a phase of Roche-lobe overflow (Savonije 1978, 1983), have well determined, circular orbits (P_{orb} of a few days), and an optical counterpart of $V \simeq 14$ mag, i.e. well within reach of VLT/UVES.

In Sect. 2 we introduce the three HMXBs. In Sect. 3 we describe the acquired observations and data reduction procedure. In Sect. 4 we present the spectral analysis and the resulting radial-velocity curves. In Sect. 5 we evaluate the measured radial-velocity amplitudes and derive the mass of the neutron star in these three systems. In Sect. 6 we summarise our conclusions and in Sect. 7 we compare these to the predictions of supernova models.

2. Eclipsing high-mass X-ray binaries; review of earlier work

Five high-mass X-ray binaries are known to host an eclipsing X-ray pulsar: Vela X−1, 4U 1538−52, SMC X−1, LMC X−4 and Cen X−3. The eclipse provides an important constraint on the orbital inclination i, an essential parameter for the mass determination. For the eclipsing X-ray source 4U 1700−37 with the O6.5 Iaf+ companion HD 153919 (Jones et al. 1973; Mason et al. 1976) no X-ray pulsations have been detected, although the compact object most likely is a neutron star (Reynolds et al. 1999; Van der Meer et al. 2005). The absence of X-ray pulsations prohibits the accurate determination of the orbital parameters of the neutron star, and thus its mass.

Van Kerkwijk et al. (1995a) present an analysis of the neutron-star mass determinations for these systems hosting an X-ray pulsar and conclude that the accuracy of the (then) available observations does not allow to discriminate between one "canonical" neutron-star mass or a mass distribution. Recent analyses of the radial-velocity curve of the wind-fed system Vela X−1 (Barziv et al. 2001; Quaintrell et al. 2003) with its B0.5 Ib companion (Hiltner et al. 1972; Vidal et al. 1973) have shown that the neutron star in this system has a mass of $1.86 \pm 0.16\ M_\odot$. Such a high neutron-star mass provides an important constraint on the EOS at supra-nuclear density.

Since the work of Reynolds et al. (1992), included in the analysis by Van Kerkwijk et al. (1995a), no new optical spectroscopy of the B0 supergiant companion (QV Nor) of 4U 1538−52 has been reported in literature. Van Kerkwijk et al. (1995a) list $1.06^{+0.41}_{-0.34}\ M_\odot$ for the mass of 4U 1538−52.

We have obtained VLT/UVES spectra of the three Roche-lobe overflow systems SMC X−1, LMC X−4 and Cen X−3. The orbital parameters (Table 1) of their X-ray pulsars are accurately known, based on X-ray pulse time delay measurements. The X-ray pulsars in these systems have short spin periods (seconds) compared to those in wind-fed systems (minutes), as the mass- and angular-momentum accretion rate in Roche-lobe overflow systems is much higher than in wind-fed systems. The photometric light curves indicate that in all three systems an accretion disc is present (Tjemkes et al. 1986; Heemskerk & Van Paradijs 1989). The X-ray eclipse duration is best measured in hard X-rays, since at lower energies the eclipses are systematically longer due to soft X-ray absorption by the stellar wind of the OB companion. The eclipse duration can thus be used to determine the radius of the OB companion.

---

[1] Recently, several new hard X-ray sources have been detected with INTEGRAL that show the characteristics of a heavily obscured HMXB with an OB-supergiant companion, called supergiant fast X-ray transients (Negueruela et al. 2006; Lutovinov et al. 2005).

2.1. SMC X−1

The B0 supergiant Sk 160 (V = 13.3 mag) is the companion to the eclipsing X-ray pulsar SMC X−1 (Schreier et al. 1972a; Liller 1973), located in the "wing" of the Small Magellanic Cloud at a distance of 60.6 kpc (Hilditch et al. 2005). The spin period of the pulsar is 0.71 s and the orbital period is 3.89 d, which is decaying on a timescale of 3×10^6 yr due to tidal inter-action (Levine et al. 1993). A super-orbital, though not strictly periodic variation of ~60 d is present in the system, most likely due to a precessing tilted accretion disc (Wojdowski et al. 1998; Clarkson et al. 2003).

The most recent determination of the radial-velocity orbit of Sk 160 has been performed by Val Baker et al. (2005). Optical spectra covering the wavelength range 4300–5100 Å were obtained with the grating spectrograph on the 1.9 metre Radcliff telescope at the Sutherland Observatory, with a resolv-ing power $R \sim 4000$. The majority of the 56 usable spectra were secured during one week of observations in September 2000. Based on a cross-correlation analysis similar to the one used by Reynolds et al. (1993), a radial-velocity amplitude of $K_{\rm opt}$ = 18.0 ± 1.8 km s^{-1} was measured, which becomes 21.8 ± 1.8 km s^{-1} when taking the effects of X-ray heating into account; the rest-frame (γ) velocity is 174 km s^{-1}. To simu-late the effects of X-ray heating, a model is used that generates velocity corrections based on contributions from different ele-ments of the projected stellar disc. The models do not take into account the presence of an accretion disc, which may well re-duce the effect of X-ray heating (Van Kerkwijk et al. 1995a). The results of Val Baker et al. (2005) are significantly differ-ent from the results obtained by Reynolds et al. (1993) who ar-rive at $K_{\rm opt}$ = 27.5 ± 1.9 km s^{-1} following a similar procedure. According to Val Baker et al. (2005), this discrepancy could be due to the limited phase coverage of the dataset of Reynolds et al. (1993) and to the fact that Reynolds et al. (1993) assume a significantly higher value for L_X when determining the non-Keplerian corrections. The latter would, however, not explain the difference in $K_{\rm opt}$ *before* applying the X-ray heating corrections. Val Baker et al. (2005) derive lower (edge-on system) and upper limits (Roche-lobe filling system) to the mass of SMC X−1 of 0.91 ± 0.08 $M_\odot$ and 1.21 ± 0.10 $M_\odot$, respectively. The mass of the optical companion is around 16.7 $M_\odot$ in both cases.

2.2. LMC X−4

After the first detection of LMC X−4 by the *Uhuru* satellite (Giacconi et al. 1972), the binary nature of its optical coun-terpart was confirmed by Chevalier & Ilovaisky (1977). The V = 14.0 mag O8 III companion (Sanduleak & Philip 1976; Kaper et al., to be submitted) is in a 1.41 d orbit (Li et al. 1978; White 1978), which is decaying on a timescale of ~500 000 yr (Levine et al. 2000). The optical light curve shows ellipsoidal variations and a super-orbital period of ~30 d due to a precess-ing accretion disc (Heemskerk & Van Paradijs 1989). The X-ray light curve includes regular eclipses as well as a pronounced flux modulation of a factor ~60 with a period of 30.5 d (Lang et al. 1981). This long-term variation is attributed to the precessing accretion disc. Kelley et al. (1983) discovered the 13.5 s X-ray pulsations of LMC X−4.

Chevalier & Ilovaisky (1977) reported on photographic spectra obtained with the 1.5 m ESO telescope from which they derived radial-velocity variations with an amplitude of 475 ± 25 km s^{-1} for the He II 4686 Å line, and a phase dependence suggesting an origin near the X-ray source.

Hutchings et al. (1978) collected 18 spectrograms using the Cassegrain image-tube spectrograph of the CTIO 4m telescope in November 1977, with an effective spectral resolution of $R \sim$ 3000. For the hydrogen lines (Hβ to H9, and an empirically determined correction to the blended Hδ line) they derive a radial-velocity amplitude of $K_{\rm opt}$ = 50 ± 5 km s^{-1}; for the He I lines $K_{\rm opt}$ = 60 ± 9 km s^{-1} is measured. For the He II 4686 Å line Hutchings et al. (1978) derive $K_{\rm opt}$ = 498 ± 14 km s^{-1}, with a phase difference compared to the H and He I absorp-tion lines of 0.79 $P_{\rm orb}$, consistent with Chevalier & Ilovaisky (1977). Kelley et al. (1983) combined the radial-velocity data of the hydrogen absorption lines presented by Hutchings et al. (1978) with measurements by Petro & Hiltner (1982) and ar-rive at $K_{\rm opt}$ = 37.9 ± 2.4 km s^{-1}. Van Kerkwijk et al. (1995a) use $K_{\rm opt}$ = 38 ± 5 km s^{-1} and obtain M_X = 1.47$^{+0.44}_{-0.39}$ $M_\odot$ and $M_{\rm opt}$ = 15.8$^{+2.3}_{-2.0}$ $M_\odot$.

2.3. Cen X−3

Cen X−3 was discovered by Chodil et al. (1967) and became the first detected binary X-ray pulsar (Giacconi et al. 1971; Schreier et al. 1972b). The V = 13.3 mag optical counterpart V779 Cen was identified by Krzeminski (1974), an O6-7 II-III star (Ash et al. 1999) in a 2.09 d circular orbit with the 4.84 s X-ray pul-sar. The optical light curve indicates the likely presence of an accretion disc, but no strong evidence is found for X-ray heating (Tjemkes et al. 1986). The X-ray light curve includes episodes of high and low X-ray flux with a characteristic timescale of 120–165 d (Priedhorsky & Terrell 1983; Paul et al. 2005).

Based on photographic spectra, Hutchings et al. (1979) derive $K_{\rm opt}$ = 24 ± 6 km s^{-1}, confirmed by Aslanov & Cherepashchuk (1982) who also report $K_{\rm opt}$ = 24 ± 6 km s^{-1}. The most recent radial-velocity measurements of V779 Cen are presented by Ash et al. (1999) who determine two very dif-ferent values of $K_{\rm opt}$ based on two datasets obtained with the 4m *Anglo-Australian Telescope* and the RGO spectrograph. The wavelength range of these spectra is 4300–4700 Å; the spectral resolution $R \sim 3000$. Ash et al. (1999) discard the results of the first dataset and arrive at $K_{\rm opt}$ = 24.4 ± 4.1 km s^{-1}. The resulting neutron-star mass is M_X = 1.21 ± 0.21 $M_\odot$ and the mass of the O-type companion $M_{\rm opt}$ = 20.5 ± 0.7 $M_\odot$.

3. Observations

We have obtained high-resolution ($R \sim 40\,000$) spectra of the three systems with UVES (Dekker et al. 2000) on the VLT in ser-vice mode in the period October 2001 to March 2002 at Paranal, Chile. The total exposure time was 17.6 h spread over 13 ex-posures of 1400 s of SMC X−1, 13 exposures of 2000 s of LMC X−4 and 12 exposures of 1600 s of Cen X−3. The in-strument was used with standard setting "390+564" and a slit width of 1.0″. This yields a wavelength range of 3580–4500 Å in the blue arm and 4625–5585 Å and 5680–6640 Å in the red arm. To determine the orbital phase of the systems we used the ephemeris of Wojdowski et al. (1998), Levine et al. (2000) and Nagase et al. (1992) for SMC X−1, LMC X−4 and Cen X−3, respectively (see Table 1). The log of observations is listed in Table 2.

In order to reduce the data to normalised spectra we used the UVES pipeline (version 1.2.0) and the ESO reduction package MIDAS (version 03SEPpl1.1). All raw echelle frames were bias and flatfield corrected. Subsequently the different orders were
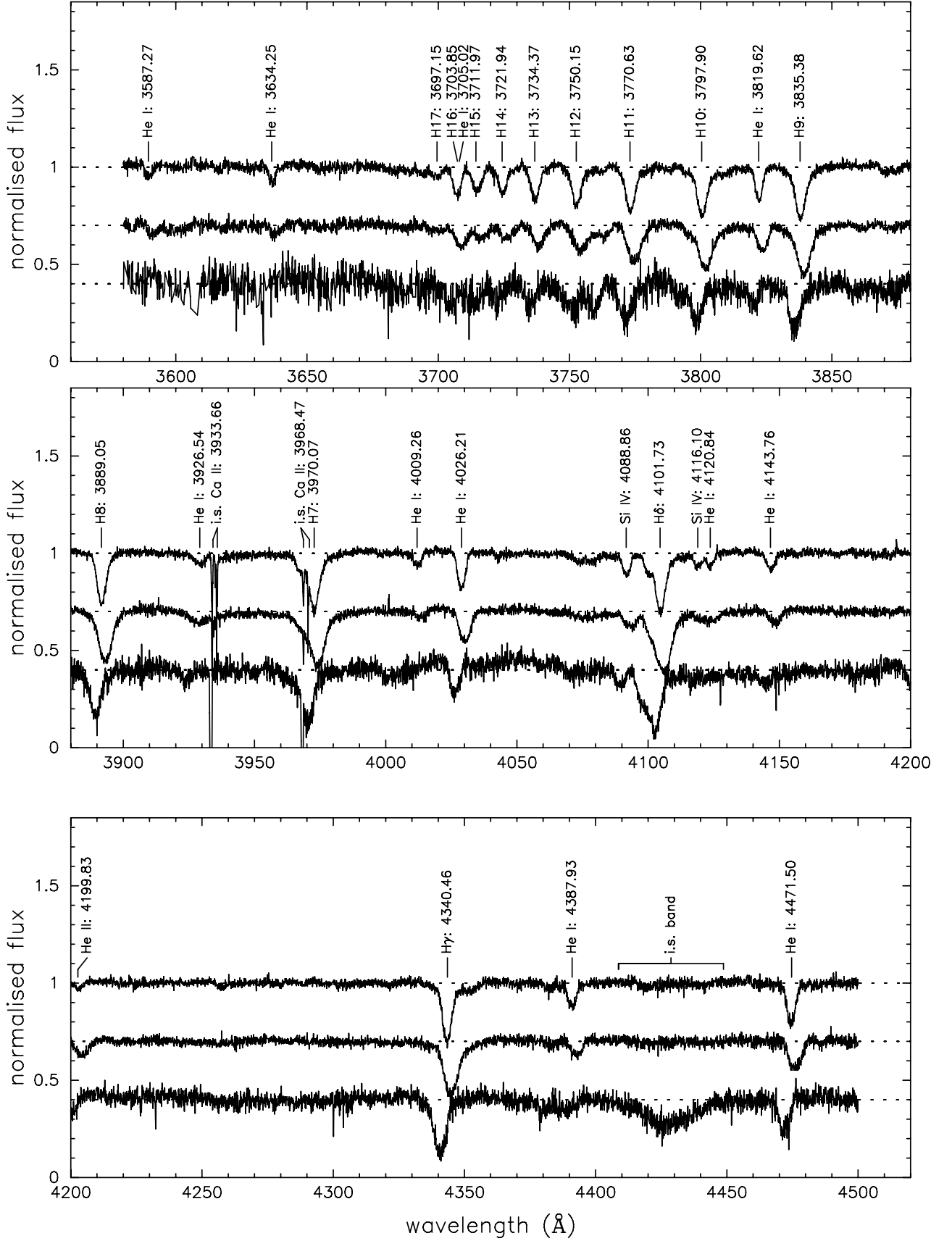
Fig. 1. Normalised spectra in the wavelength range 3580–4500 Å of SMC X−1 at orbital phase ϕ = 0.06 (*top spectrum*), LMC X−4 at orbital phase ϕ = 0.04 (*middle spectrum*) and Cen X−3 at orbital phase ϕ = 0.09 (*bottom spectrum*), respectively. The line identifications are shown above the spectrum of SMC X−1. Note that the reddening of Cen X−3 ($E(B − V) \sim 1.4$) clearly affects the S/N in this wavelength range.
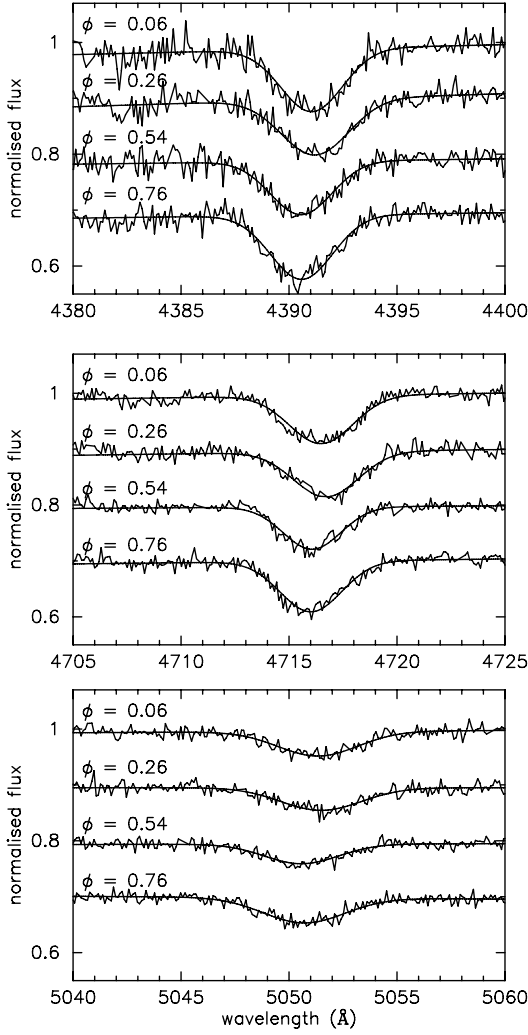
Fig. 4. Example of Gaussian fits for the He I line at 4387.93 Å (*upper panel*), the He I line at 4713.17 Å (*middle panel*) and the He I line at 5047.74 Å (*lower panel*) in the spectrum of the B supergiant companion to SMC X−1. The spectra and the Gaussian fits are shown at four different quadratures. To better visualise the fits the spectra are smoothed. Note that the Gaussian profile fits represent the rotationally broadened line profiles very well. Furthermore, the orbital motion of the B supergiant companion is easily observed.

extracted using the optimal extraction routine available within the UVES pipeline. High signal-to-noise ($S/N \gtrsim 50$) spectra extracted with this routine show a ripple effect. In our spectra this effect is only marginally present in some spectra of SMC X−1 in the wavelength range 5100–5585 Å. This range contains the He II 5411.53 Å line, but we do not use it for the determination of the radial-velocity amplitude of the system (Sect. 4.2).

Cosmic ray hits were removed by rejecting the affected wavelength bins and subsequent interpolation. After this, the spectra were normalised by fitting the continuum with a spline over the whole wavelength range of one spectral arm. The normalised spectra of the three systems are shown in Figs. 1 to 3.

We verified the long-term stability of UVES by measuring the position of the interstellar lines of Ca II K at 3933.66 Å, Ca II H at 3968.47 Å, Na I D1 at 5895.92 Å and Na I D2 at 5889.95 Å for all spectra. This resulted in a deviation of less than 1 km s^{-1} throughout the whole observing period of each system, i.e. several months.
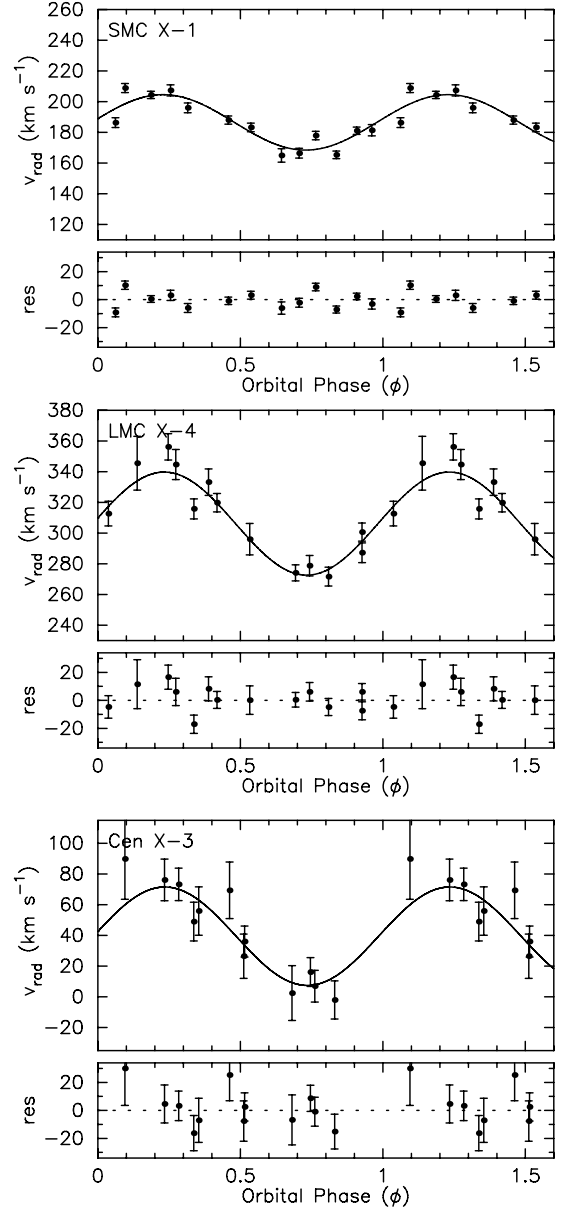

Fig. 5. Example of radial-velocity curves obtained from the H13 line at 3734.37 Å. Some datapoints are shown twice to better visualise trends with orbital phase. The error bars indicate 1σ errors. The lower panels show the residuals of the fit.

4. Spectral analysis

To obtain a radial-velocity measurement often the complete spectrum is cross-correlated with a template spectrum. This approach has many advantages when using spectra with relatively low spectral resolution and poor signal-to-noise. In our case the spectra are of such high quality that the radial-velocity amplitude can be determined for each line separately. The advantage of such a strategy is that it is possible to assess the influence of possible distortions due to e.g. X-ray heating and gravity darkening, as in these systems the OB star is irradiated by a powerful X-ray source ($L_{opt} \simeq L_X$) and is filling its Roche-lobe. Furthermore, the extended OB-star wind is focused into a shadow wind which possibly produces a strong shock (a so-called photo-ionisation wake, see e.g. Blondin 1994; Kaper et al. 1994) where the fast shadow wind catches up with the stagnant flow inside the X-ray
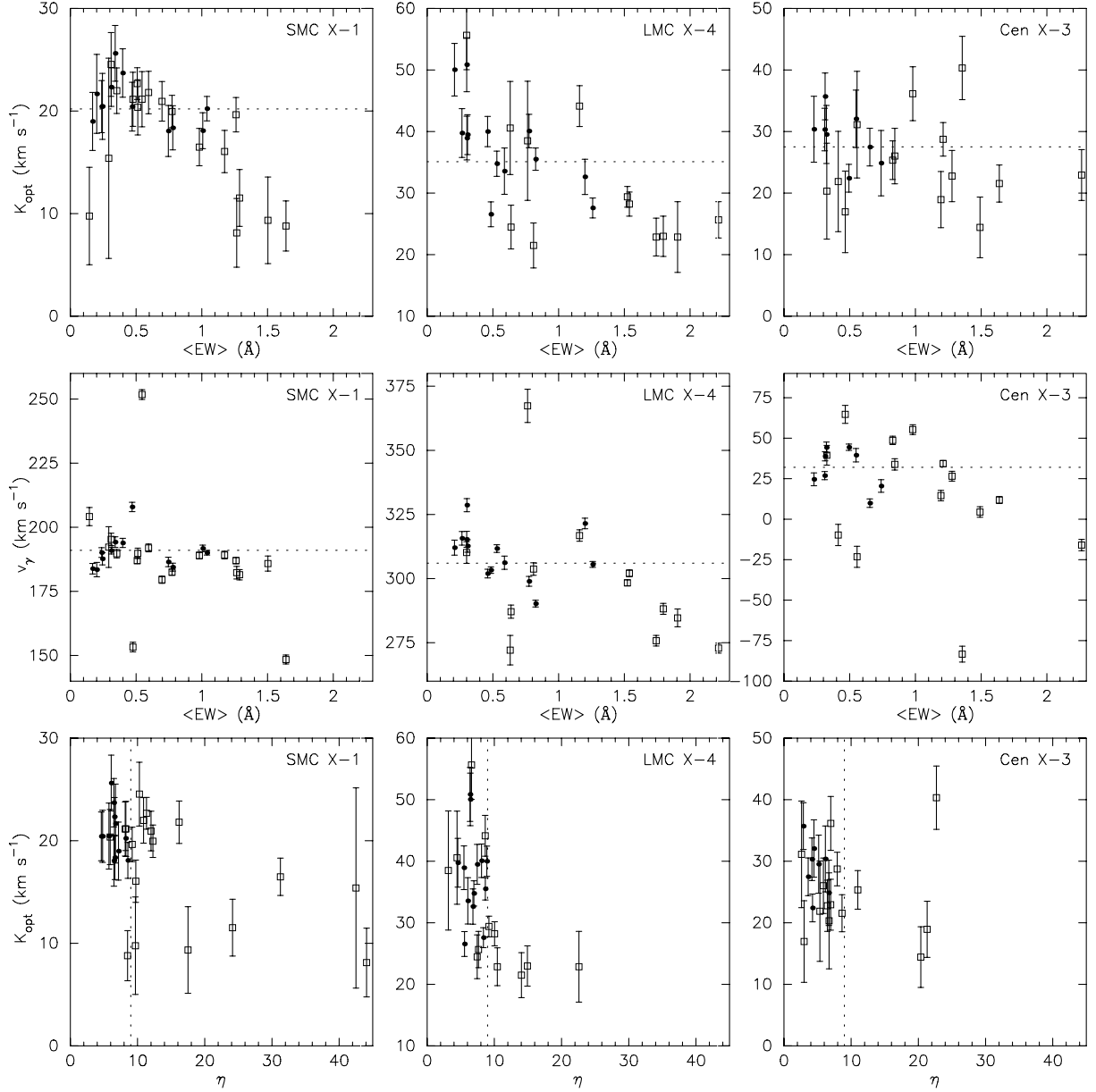
Fig. 6. *The upper panels* show the radial-velocity amplitude (K_{opt} in km s^{-1}) measured for a given line as a function of its mean line equivalent width ($\langle EW \rangle$). The error bars indicate 1σ errors. Especially for SMC X−1 a clear trend is visible with line strength: for large mean EW K_{opt} is systematically lower. The finally adopted K_{opt} is represented by the horizontal dotted line. *The middle panels* show the γ-velocity and *the bottom panels* show K_{opt} as a function of the line variability parameter η; lines with $\eta > 9$ are rejected (see text for motivation). The lines that are rejected because of this and other criteria (such as blending) are represented by open squares. The filled circles indicate the lines that are used to determine the (mean) radial-velocity amplitude. These selections show less spread in K_{opt}.

ionization zone. The shadow wind and photo-ionization wake induce orbital modulations of spectral lines formed in the stellar wind (i.e. strong spectral lines such as the first lines of the Balmer series and the strongest helium lines).

Figures 1 to 3 show that the spectra contain mostly lines that are identified with transitions from H and He I. Only a few He II lines and some metal lines are detected, consistent with the modest metallicity of the Magellanic Clouds and OB supergiant spectral types. We show the spectra observed near X-ray eclipse (orbital phase $\phi \sim 0.0$). Some of the lines are blended or show a slight asymmetry. A comparison of the spectra obtained at different orbital phase reveals that several lines also vary in line strength. Still, Fig. 4 demonstrates that many lines are well represented by a Gaussian profile (i.e. as one would expect for a

rotationally broadened profile). Therefore, Gaussian profiles are fit to all individual lines to determine the radial-velocity curve (Sect. 4.1). Subsequently, the observed line profiles are examined on asymmetry and variations with orbital phase (Sect. 4.2).

4.1. Radial-velocity curves

We determine the line centre, and thus the Doppler shift with respect to the heliocentric restframe, by fitting the profile with a Gaussian. The Gaussian sets the full-width at half maximum (FWHM), the central line depth and the central wavelength of the profile, i.e. three free parameters. A χ^2 minimalization procedure delivers the best fit Gaussian profile and defines the

Table 3. List of lines that have been fitted with a Gaussian. The rest wavelength of the line is given as well as the mean equivalent width (EW, in Ångström) with its 1σ error. The magnitude of the variations in line EW is expressed as the ratio η of the standard deviation of the line EW to the error on the mean EW. Rejected lines are indicated with a remark: lines marked with an "B" are blends; a "V" stands for lines exhibiting strong EW variations ($\eta > 9$); a number (e.g. 0.5) indicates a deviation in the EW at that orbital phase. Electronic tables that contain the radial-velocity amplitude, EW and FWHM variations for each line are available as on-line material at the CDS.

Identification	$\lambda_{\rm rest}$ (Å)	SMC X−1 $\mu_{\rm EW}$ (Å)	η	Remarks	LMC X−4 $\mu_{\rm EW}$ (Å)	η	Remarks	Cen X−3 $\mu_{\rm EW}$ (Å)	η	Remarks
H Balmer series										
Hβ	4861.33	1.265(4)	44.1	V,0.5	1.905(7)	22.6	V,0.5	1.491(6)	20.4	V,0.5
Hγ	4340.46	1.287(5)	24.2	B,V,0.5	1.796(8)	14.9	B,V,0.5	1.638(10)	8.6	B,0.5
Hδ	4101.73	1.503(7)	17.5	B,V,0.5	2.216(9)	7.6	B,V,0.5	2.264(16)	7.0	B,0.5
Hϵ	3970.07	1.640(13)	8.5	B,0.5	1.742(11)	10.4	B,V,0.5	1.356(23)	22.7	B,V,0.5
H8	3889.05	1.173(4)	9.7	V,0.5	1.538(6)	10.0	V,0.5	1.278(11)	6.5	0.5
H9	3835.38	1.260(5)	9.2	B?,V,0.5	1.523(7)	9.2	B?,V	1.211(12)	7.9	B?,0.5
H10	3797.90	1.039(5)	8.2		1.259(7)	8.4		0.843(12)	5.9	0.5
H11	3770.63	1.007(6)	8.6		1.200(10)	6.8		0.980(18)	7.0	0.5
H12	3750.15	0.779(6)	6.6		0.638(10)	7.4	B	0.413(15)	5.3	B
H13	3734.37	0.745(6)	6.5		0.588(12)	6.1		0.548(22)	4.5	
H14	3721.94	0.513(8)	5.9	B	–	–		–	–	
H15	3711.97	0.470(11)	4.6		–	–		–	–	
H16	3703.85	0.545(8)	8.3	B	0.764(237)	3.1	B	0.466(96)	3.0	B
He I 3P-3D series										
He I 2p-3d	5875.66	0.981(5)	31.3	V,0.0	1.159(11)	8.6	0.0	1.194(7)	21.3	V,0.0,0.5
He I 2p-4d	4471.50	0.773(6)	12.3	V,0.0	0.775(8)	8.1		0.739(10)	6.7	
He I 2p-5d	4026.21	0.697(4)	12.1	V,0.0	0.825(5)	8.7		0.653(8)	3.6	
He I 2p-6d	3819.62	0.509(4)	11.3	V,0.0	0.460(5)	8.9		0.313(10)	2.9	
He I 2p-7d	3705.02	0.476(9)	8.2	B,0.0	0.632(66)	4.4	B	0.556(152)	2.6	B
He I 2p-8d	3634.25	0.244(5)	5.7		0.208(7)	6.4		–	–	
He I 2p-9d	3587.27	0.169(5)	7.2		–	–		–	–	
He I 1P-1D series										
He I 2p-4d	4921.93	0.595(3)	16.2	V,0.0	0.530(5)	7.0		0.323(5)	5.2	
He I 2p-5d	4387.93	0.398(5)	6.5		0.302(6)	5.5		–	–	
He I 2p-6d	4143.76	0.341(4)	6.1		0.301(6)	6.4		–	–	
He I 2p-7d	4009.26	0.238(4)	4.8		–	–		–	–	
He I 3P-3S series										
He I 2p-4s	4713.17	0.311(4)	6.6		0.265(5)	4.6		0.228(6)	6.2	
He I 1S-1P series										
He I 2s-3p	5015.68	0.353(3)	10.9	V,0.0	0.307(5)	7.4		0.310(5)	4.2	
He I 1P-1S series										
He I 2p-4s	5047.74	0.201(4)	6.7		–	–		–	–	
Other lines										
He II 4-7	5411.53	0.292(4)	42.5	V,0.5	0.809(7)	14.0	V,0.5	0.827(5)	11.0	B,0.5
He II 4-11	4199.83	0.145(5)	9.7	V,0.5	0.485(7)	5.6		0.494(9)	4.2	
Si IV 4s-4p	4088.86	0.310(4)	10.3	V,0.0	0.300(11)	6.6	B	0.326(12)	6.7	B

accuracy of the fit parameters. Emission-line profiles, such as Hα, are not included in the fitting procedure.

The orbital parameters are accurately known from X-ray pulse time delay measurements (see Table 1). We assume the orbit to be circular, since in all cases the eccentricity $e \lesssim 0.008$. The remaining free parameters describing the radial-velocity curve are the radial-velocity amplitude, $K_{\rm opt}$, and the restframe velocity of the system, v_γ. In principle, a small shift in orbital phase could be present due to the inaccuracy of the orbital period, the period derivative, and mid-eclipse time (Table 1). The measured orbital phase shifts are not significantly different from zero, but are slightly larger than the phase shifts one may expect based on the accuracy of the ephemeres of these systems. The phase shift should be the same for all lines and has to be fixed to the average value during a second iteration.

A radial-velocity curve is obtained for each individual line; Fig. 5 displays for each system a radial-velocity curve representative for the spectral lines used to measure the radial-velocity amplitude. Note that the data points were obtained from several orbits of the system; the dozen spectra per system are evenly distributed with orbital phase, thanks to the service-mode observations allowing to obtain spectra spread over a period of more than one month.

Figure 6 indicates that $K_{\rm opt}$ and v_γ show quite some dispersion when comparing the radial-velocity curves of individual lines. $K_{\rm opt}$ shows a dependence on line strength and line variability, diagnostics that we will use to reject lines when determining the mean radial-velocity amplitude used to calculate the mass of the neutron star.

4.2. Line selection

As our observational strategy is aimed at the derivation of the radial-velocity curve based on individual lines, we select only lines that are well identified. Also, all lines that are (partially)
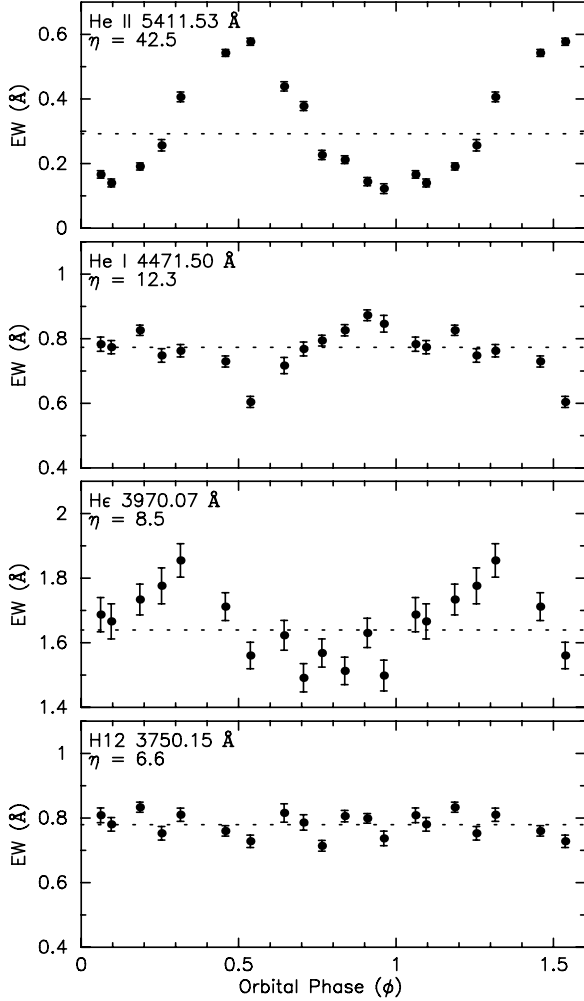
Fig. 7. Equivalent width (EW) variations with orbital phase (ϕ) observed in SMC X−1. The error bars indicate 1σ errors and the dotted line the average value. Some datapoints are shown twice to better visualise trends with orbital phase. The value of the defined line variability parameter η is indicated for each line. The upper panel shows the large variations in the He II line at 5411.53 Å, the second panel shows the inverse behaviour of the He I line at 4471.50 Å, the third panel shows the variations of Hϵ at 3970.07 Å. A stable line is shown in the lower panel, i.e. the H12 line at 3750.15 Å. The EW ratio of the He II and He I lines is sensitive to $T_{\rm eff}$ and can be used for spectral classification; apparently, the spectral type of SMC X−1 varies with orbital phase. The variations are consistent with being caused by X-ray heating of the stellar surface facing the X-ray source.

Fig. 8. Full width at half maximum (FWHM) variations of the Hγ line at 4340.46 Å (*upper panel*) and the He I line at 4387.93 AA (*lower panel*) of SMC X−1 as a function of orbital phase (ϕ) in km s^{-1}. The error bars indicate 1σ errors and the dotted line the average value. Some datapoints are repeated once to better visualise trends with orbital phase. A maximum in FWHM is clearly seen around $\phi \sim 0.25$; a second, though much less pronounced maximum is visible at $\phi \sim 0.75$. Such FWHM variations are also detected in other lines, as well as in the systems LMC X−4 and Cen X−3.

blended, are rejected. In Table 3 this is indicated with a "B" as a remark.

In these high-mass X-ray binaries it is expected that at least some lines in the OB-star spectrum are affected by the presence of the X-ray pulsar companion (see e.g. Van Paradijs et al. 1978; Reynolds et al. 1993). In principle, one could model the photospheric line profiles of the OB supergiant companion by calculating a grid of many (thousands) surface elements, adopting for each surface element an intrinsic line profile, and obtaining the integrated line profile by a weighted integration of the (mainly by stellar rotation) Doppler-shifted intrinsic profiles of all visible surface elements. Such computationally demanding techniques have been successfully explored in stellar pulsation studies (e.g. Schrijvers et al. 1997) and in modeling photometric lightcurves of HMXBs (e.g. Heemskerk & Van Paradijs 1989).
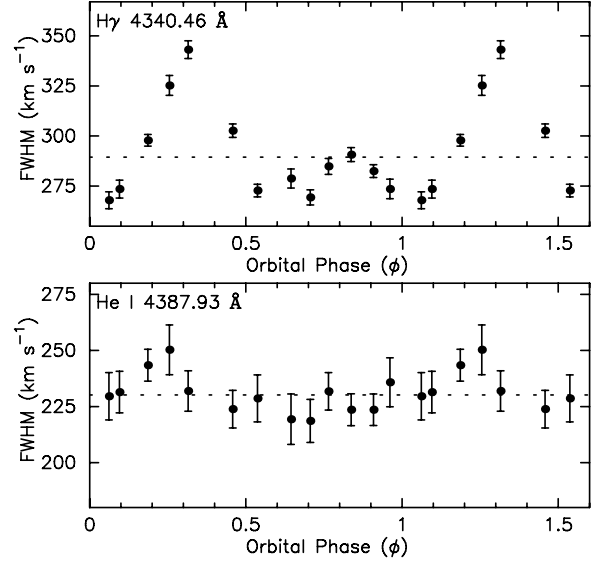
Also, variations in the intrinsic line profiles due to variations of surface temperature and gravity have been included (Schrijvers & Telting 1999), so that one could apply such a method to the case of an OB supergiant irradiated and deformed by a close and compact X-ray source. Although we have now made an advance in analysing spectra of the OB companions to X-ray pulsars by studying individual lines rather than cross-correlating complete spectra, we consider this modeling effort beyond the scope of the present paper, even though it has the potential to deliver very important information on the interpretation and analysis of the obtained spectra.

A first step in this direction has been undertaken by Abubekerov et al. (2004); they model the line formation process taking X-ray heating and gravitational darkening into account. As the luminosity distribution and shape of the star are altered, the measured radial velocity, as well as the line equivalent width, depend on the depth of the line-forming region and orbital phase. Abubekerov et al. (2004) show that these effects will result in a reduction of the derived radial-velocity amplitude by several km s^{-1}.

That these effects manifest themselves in our observations is nicely demonstrated by the large EW variations of the He II line at 5411.53 Å of SMC X−1 (see Fig. 7). This line varies with about a factor ~ 5 in EW and reaches a maximum EW near $\phi \sim 0.5$. The He I line at 4471.50 Å (and also He I 5875.66 Å) shows the opposite behaviour and has a minimum strength at this orbital phase (see Fig. 7). Since a He I / He II line ratio is sensitive to $T_{\rm eff}$ it can be used for spectral classification; however, traditionally the ratio of He I 4471 over He II 4541, accessible in the blue spectrum, is used for spectral classification (Conti & Alschuler 1971; Lennon et al. 1993; Mokiem et al. 2005). Line ratios involving the He I 5876 and He II 5412 lines have not (yet) been calibrated (Mokiem, priv. comm.). The observed variations in line ratio indicate a higher $T_{\rm eff}$ at the side of the OB

Table 4. Final selection of lines that is used for the determination of the radial-velocity amplitude (K_{opt}) for each system. The three fit parameters are listed, i.e. the system velocity (v_γ), K_{opt}, and a phase shift ($\Delta\phi$). The goodness of the fit is expressed as χ_r^2. All errors are 1σ.

λ_{rest} (Å)	SMC X−1				LMC X−4				Cen X−3			
	v_γ	K_{opt}	$\Delta\phi$	χ_r^2	v_γ	K_{opt}	$\Delta\phi$	χ_r^2	v_γ	K_{opt}	$\Delta\phi$	χ_r^2
3797.90	190.0 ± 0.9	20.2 ± 1.2	0.01(1)	2.6	305.5 ± 1.1	27.6 ± 1.6	0.01(1)	1.6	−	−	−	−
3770.63	191.7 ± 1.3	18.1 ± 1.8	0.01(2)	3.8	321.5 ± 2.1	32.6 ± 2.9	−0.02(2)	3.2	−	−	−	−
3750.15	184.5 ± 1.6	18.4 ± 2.2	0.04(2)	4.3	−	−	−	−	−	−	−	−
3734.37	186.5 ± 1.8	18.1 ± 2.5	0.02(2)	4.9	306.2 ± 2.6	33.6 ± 3.8	0.02(2)	1.7	39.5 ± 4.1	32.1 ± 4.7	0.02(4)	0.9
3711.97	207.9 ± 1.8	20.4 ± 2.4	0.07(2)	0.9	−	−	−	−	−	−	−	−
4471.50	−	−	−	−	298.9 ± 1.9	40.1 ± 2.7	0.00(1)	2.7	20.5 ± 3.9	24.9 ± 5.3	0.08(4)	5.8
4026.21	−	−	−	−	290.2 ± 1.3	35.5 ± 1.8	0.00(1)	2.9	9.9 ± 2.6	27.5 ± 3.1	0.03(3)	3.3
3819.62	−	−	−	−	301.9 ± 1.7	40.0 ± 2.5	−0.01(1)	2.0	38.8 ± 2.8	35.7 ± 3.8	0.07(2)	0.7
3634.25	187.7 ± 2.4	20.5 ± 3.2	0.03(3)	2.0	312.1 ± 2.9	50.0 ± 4.3	−0.03(2)	0.8	−	−	−	−
3587.27	183.9 ± 2.1	19.0 ± 2.8	0.01(3)	1.0	−	−	−	−	−	−	−	−
4921.93	−	−	−	−	311.7 ± 1.5	34.8 ± 2.1	−0.02(1)	1.8	44.3 ± 3.3	29.5 ± 4.7	0.10(3)	3.0
4387.93	193.9 ± 1.8	23.7 ± 2.4	0.04(2)	3.1	328.6 ± 2.6	38.9 ± 3.6	−0.01(2)	1.4	−	−	−	−
4143.76	194.2 ± 2.1	25.6 ± 2.7	0.02(2)	3.7	315.3 ± 3.1	50.9 ± 4.4	−0.01(2)	1.6	−	−	−	−
4009.26	190.1 ± 1.9	20.4 ± 2.5	0.05(2)	1.8	−	−	−	−	−	−	−	−
4713.17	190.9 ± 1.3	22.3 ± 1.9	0.02(1)	2.3	315.7 ± 2.7	39.8 ± 4.0	0.00(2)	1.7	24.6 ± 4.0	30.4 ± 5.4	0.08(3)	1.6
5047.74	183.5 ± 2.8	21.7 ± 3.9	0.03(3)	3.0	−	−	−	−	−	−	−	−
5015.68	−	−	−	−	312.7 ± 2.4	39.5 ± 3.2	−0.03(2)	2.1	26.9 ± 2.5	30.3 ± 3.5	0.09(2)	1.7
4199.83	−	−	−	−	303.3 ± 1.3	26.6 ± 2.0	0.05(1)	0.6	44.4 ± 2.0	22.4 ± 2.3	0.03(2)	0.8

star facing the X-ray source, and is evidence for X-ray heating in SMC X−1. As a consequence, the spectral type of the optical companion to SMC X−1 changes as function of binary aspect angle. A similar effect has been observed in the optical spectrum of V779 Cen, the O6 companion of Cen X−3 (Hutchings et al. 1979).

The derived value of the radial-velocity amplitude shows a dependence on line strength (Fig. 6). Furthermore, the observed *variations* in EW also increase with line strength. As illustrated above, these variations likely reflect distortions of the line forming region due to e.g. X-ray heating and the (disturbed) stellar wind. Since K_{opt} should be a unique value, we investigate whether a selection criterion can be defined to reject lines that are affected by these distortions and thus do not yield a sound measurement of K_{opt}.

To measure these distortions we apply a velocity moment analysis, with which one can determine the equivalent width (EW), central velocity, standard deviation (σ) and skewness (τ) of a given line. The nth moment (μ_n) of a distribution $f(v)$ in velocity v is given by:

$$\mu_n = \frac{\int v^n f(v) \, dv}{\int f(v) \, dv},\tag{1}$$

and

$$\mu_0 = \int f(v) \, dv.\tag{2}$$

For such a distribution the EW is proportional to μ_0 and the central velocity to μ_1. The standard deviation (σ) and skewness (τ) are often defined as:

$$\sigma^2 = \frac{\int (v - \mu_1)^2 f(v) \, dv}{\mu_0},\tag{3}$$

and

$$\tau = \frac{\int (v - \mu_1)^3 f(v) \, dv}{\mu_0 \, \sigma^3},\tag{4}$$

in which the skewness (τ) is a measure of the asymmetry of the distribution. For a Gaussian profile the skewness τ is zero; if $\tau \neq 0$ the spectral line is not well represented by a Gaussian. If so, one can not use a gaussian to fit the line in order to measure its radial velocity, as we did in Sect. 4.1. It turns out that for the lines that are not blended, τ is consistent with being equal to zero within the error. Note, however, that the error on τ is too large to measure any significant deviations from zero, because it depends on the error on μ and σ to the third power (see Eq. (4)). The EW and central velocity (first moment) are much more accurately determined and are consistent with the respective values derived from the gaussian profile fits.

For each line we determine whether the line EW varies significantly by comparing the deviation in EW to the error on the mean EW (Table 3). Note that these values are not equal; the error on the mean depends on the error in EW of the individual spectra, while the standard deviation is the spread in the *distribution* of EWs. Since the strongest lines are formed in the outer layers of the stellar photosphere and/or in the extended stellar wind these lines are expected to be most affected by X-ray heating, gravity darkening, etc., and will thus show intrinsic variations when the system revolves. The observed trend in K_{opt} with v_γ (Fig. 6) also indicates that the stronger lines are formed further out in the stellar atmosphere and wind (an effect called Balmer progression, see e.g. Crampton et al. 1985; Abubekerov et al. 2004). We define a line variability parameter η to formulate a selection criterion (Table 3). This parameter is defined as the ratio of the standard deviation of the EW variations to the error on the mean EW. The main motivation behind this definition is that the EW is in principle not sensitive to radial-velocity variations, i.e. the key parameter that we want to measure in the spectra. However, η turns out to be an accurate probe of intrinsic line profile variability. Other methods to measure line profile variability (e.g. the temporal variance spectrum analysis method introduced by Fullerton et al. 1996) are sensitive to radial-velocity variations.

We select $\eta = 9$ as the value above which lines are rejected. These lines are indicated with a "V" in Table 3. The threshold value for η is chosen arbitrarily, but is a reproducable and objective means to quantify line profile variations. As it is an averaged quantity, the η threshold does not reject lines exhibiting only modest EW variations and having relatively large errors on

the measured EWs (e.g. the Hϵ at 3970.07 Å shown in Fig. 7). On the other hand, it does reject some lines that have highly accurately determined EWs and that exhibit hardly any EW variations with orbital phase. To test the impact of the chosen value for the η threshold on the obtained value of the radial-velocity amplitude, we have evaluated the results for different values of η. Including all lines for which $\eta < 8$ then K_{opt} is 20.8 ± 1.5, 35.7 ± 1.8, and 27.5 ± 2.3 km s^{-1} for SMC X−1, LMC X−4, and Cen X−3, respectively. Similarly, we obtain 20.0±1.2, 34.2±1.3, and 26.2±2.7, respectively, if we select the lines with $\eta < 13$. As expected, we obtain a lower value of K_{opt} for a higher value of η, and vice versa, while the error on the result increases when including lines that show more intrinsic variations. Still, the values for K_{opt} agree within the error for the applied range in η.

We now fix the threshold to $\eta = 9$; to ensure that the lines with $\eta < 9$ and small variations concentrated around $\phi \sim 0.0$ or $\phi \sim 0.5$, are rejected, we mark these in Table 3 listing the orbital phase at which these variations are concentrated. Note that most of these lines are already marked with a "V", i.e. rejected based on the η threshold.

The full width at half maximum (FWHM) of the line also varies as a function of orbital phase ϕ. This behaviour is especially visible in the Balmer series lines of hydrogen, most prominent in the stronger lines. Figure 8 shows that the FWHM increases when the system revolves from X-ray eclipse to $\phi \sim 0.25$, where it reaches a maximum before declining again. At $\phi \sim 0.75$ another, though smaller increase in FWHM is detected. The helium (and some other metallic) lines also show FWHM variations, but less pronounced and not as periodic as observed in the hydrogen lines. Furthermore, these FWHM variations are best seen in SMC X−1 and LMC X−4, but are less clear in Cen X−3.

Apparently, if one would use these lines to determine the (projected) stellar rotation velocity, one would arrive at a larger value of $v \sin i$ when the system is looked upon from a side view. This may be due to the elongated shape of the star as it is filling its Roche lobe, as evidenced by the observed ellipsoidal variations. The dependence on line strength would be explained by the fact that the line forming region is further out in the atmosphere when the line is stronger. This would, however, not explain the difference in amplitude of this effect observed between $\phi \sim 0.25$ and $\phi \sim 0.75$.

Differences in spectral appearance when comparing spectra obtained at $\phi \sim 0.25$ and $\phi \sim 0.75$ are well known to occur in spectroscopic binaries. The "Struve-Sahade" effect (Struve 1937; Sahade 1962) is the apparent strengthening of the secondary spectrum of a hot binary when the secondary is approaching and the corresponding weakening of the lines when it is receding (see Gies et al. 1997, for an observational overview). The cause of this effect may be the presence of a gas stream (bow shock, wind collision) trailing the secondary in its orbit (Sahade 1959; Gies et al. 1997). Hydrodynamical simulations of SMC X−1 by Blondin (1994) indicate that a collision of wind material from the shadow wind with material in the X-ray ionisation zone is present in the system. Perhaps that this shocked material introduces the difference in amplitude observed in the FWHM of the strong Balmer lines that are formed in the stellar wind.

As we do not have a clear explanation for these variations in FWHM, we investigate the possible influence of this effect on the determination of K_{opt}. Note that the stronger Balmer lines are already excluded from the radial-velocity analysis on the basis of the EW variations. We fix the FWHM on its mean value, its maximum and its minimum and refit the lines. It turns out that the

measurement of the centre of the line profile is not affected much by these FWHM variations. The derived radial-velocity amplitude, K_{opt}, is the same within its errors in all cases. Therefore, we decide not to exclude more lines based on a FWHM variation criterion (most of the lines showing this effect were excluded on other grounds anyway).

4.3. Radial-velocity amplitude

Table 4 shows the final selection of lines for which good fits to the radial-velocity curve are obtained, resulting in a measurement of K_{opt} and v_γ. Since the phase shift should be equal for all lines in one system, we refit all lines with the phase shift fixed to the weighted average, i.e. $\triangle\phi$ is 0.026, –0.003, and 0.065 for SMC X−1, LMC X−4, and Cen X−3, respectively. Fixing these values does not influence the other parameters much; they are the same within their errors.

To avoid systematic errors while determining the final mean value of K_{opt} we shift all determined line centres to equal v_γ. The weighted mean values of v_γ are 191 ± 6 km s^{-1}, 306 ± 10 km s^{-1} and 32 ± 13 km s^{-1} for SMC X−1, LMC X−4 and Cen X−3, respectively. Then we calculate the weighted mean of the radial velocity for each spectrum (see Table 5). The average dataset we fit in the same way as the individual lines, which results in the three radial-velocity curves shown in Fig. 9. The goodness of the fits with respect to the number of degrees of freedom (d.o.f.) are χ_r^2/d.o.f = 9.8/12, χ_r^2/d.o.f = 9.1/12 and χ_r^2/d.o.f = 7.2/11 for SMC X−1, LMC X−4 and Cen X−3, respectively. The error bars indicate 1σ errors multiplied by χ_r to obtain a $\chi_r^2 = 1$. The residuals to the fit do not show any further evidence for systematic effects with orbital phase, as is the case for e.g. Vela X−1 (Van Kerkwijk et al. 1995b; Barziv et al. 2001). The final values of K_{opt} are 20.2 ± 1.1 km s^{-1}, 35.1 ± 1.5 km s^{-1} and 27.5 ± 2.3 km s^{-1} for SMC X−1, LMC X−4 and Cen X−3, respectively. The accuracy of the determination of K_{opt} has been significantly improved (by a factor 2–4) compared to previous measurements (and comparable to and consistent with Val Baker et al. (2005) in the case of SMC X−1). These values are subsequently used to calculate the mass of the optical companion and the X-ray source.

5. The neutron star masses

In order to measure the mass of the neutron star and its optical companion we apply the mass function. For an orbit with eccentricity e it can be shown that this is defined as:

$$M_{opt} = \frac{K_X^3 P \left(1 - e^2\right)^{\frac{3}{2}}}{2\pi G \sin^3 i} \left(1 + q\right)^2 \tag{5}$$

and

$$M_X = \frac{K_{opt}^3 P \left(1 - e^2\right)^{\frac{3}{2}}}{2\pi G \sin^3 i} \left(1 + \frac{1}{q}\right)^2, \tag{6}$$

where M_{opt} and M_X are the masses of the optical component and the X-ray source, respectively, K_{opt} and K_X are the semi-amplitudes of the radial-velocity curve, P is the period of the orbit and i is the inclination of the orbital plane to the line of sight. The mass ratio q is defined as:

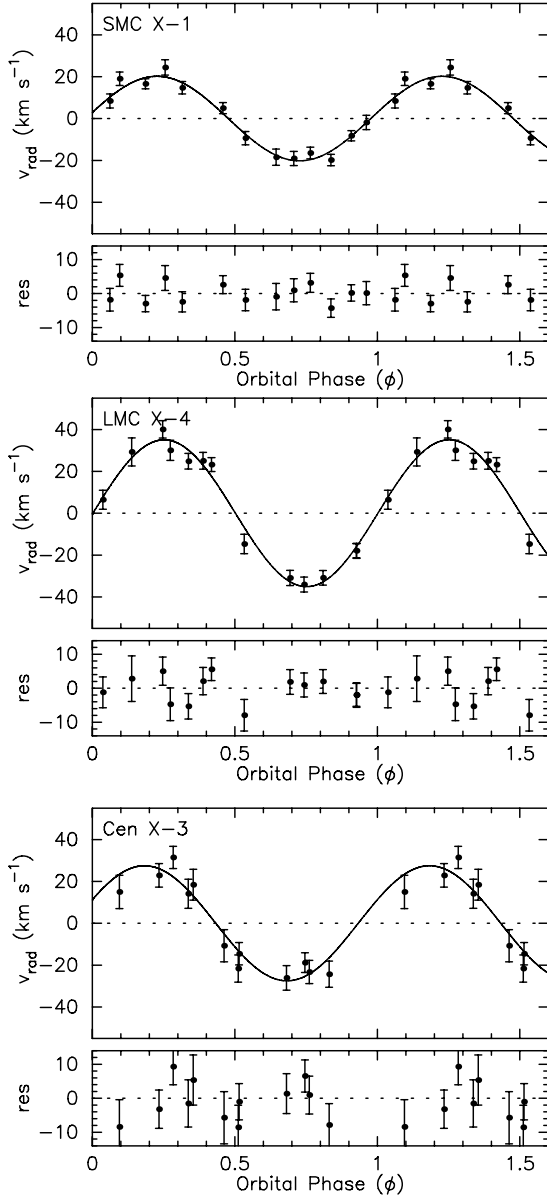$$q = \frac{M_X}{M_{opt}} = \frac{K_{opt}}{K_X}. \tag{7}$$

Fig. 9. Radial-velocity curves obtained from weighing the radial velocities of all selected lines per observation. Some datapoints are shown twice to better visualise trends with orbital phase. The error bars indicate 1σ errors multiplied by χ_r to obtain a $\chi_r^2 = 1$. Note that v_γ has been set to zero.

The values for K_X and P can be obtained very accurately from X-ray pulse timing delay measurements (Wojdowski et al. 1998; Levine et al. 2000; Nagase et al. 1992). The VLT/UVES spectra provide a value for K_{opt}. For the determination of the inclination of the system we follow the approach of Rappaport & Joss (1983), who showed that:

$$\sin i \approx \frac{\sqrt{1 - \beta^2 \left(\frac{R_L}{a}\right)^2}}{\cos \theta_e} \qquad (8)$$

where R_L is the Roche-lobe radius of the optical component, β is the ratio of the radius of the optical component to R_L (i.e. a Roche-lobe filling factor), a is the separation of the centres of mass of the two components, and θ_e is the semi-eclipse angle of the compact object (see also Joss & Rappaport 1984, for a review on mass determinations in X-ray binaries).

The ratio of the Roche-lobe radius and the orbital separation can be approximated by:

$$\frac{R_L}{a} \approx A + B \log q + C \log^2 q. \qquad (9)$$

The values of the constants A, B and C were determined by Rappaport & Joss (1983) to be:

$$A \approx 0.398 - 0.026\Omega^2 + 0.004\Omega^3 \qquad (10)$$

$$B \approx -0.264 + 0.052\Omega^2 - 0.015\Omega^3 \qquad (11)$$

$$C \approx -0.023 - 0.005\Omega^2, \qquad (12)$$

where Ω is the ratio of the rotational frequency of the optical companion to the orbital frequency of the system; in case of synchronous rotation $\Omega = 1$. However, the timescale at which these systems are expected to synchronise is slightly longer than the timescale at which the orbit will circularise (for a detailed description see e.g. Hut 1981). Therefore, these systems may still be in the process of synchronising the optical companion to the orbit, whereas their orbits have already become circular. The fact that the orbital periods of all three systems are decreasing, suggests that the donor stars are rotating slower than synchronous and that tidal forces are transferring orbital angular momentum to synchronise the system.

It is possible to determine Ω by measuring the projected rotational velocity $v_{rot} \sin i$ of the OB companion using the spectra at $\phi = 0.0$. We use the grid of unified stellar atmosphere/wind models of early-type supergiants computed by Lenorzer et al. (2004) using CMFGEN (Hillier & Miller 1998). First we select the lines that correspond to lines included in the model. Subsequently, we select the model atmosphere that reproduces the observed line spectrum best. The normalised flux of the model is then scaled to yield exactly the observed EW. The models that correspond best to our selection of lines are named "AR1Ia", "AR1III" and "O9III-AR2III" for SMC X−1, LMC X−4 and Cen X−3, respectively by Lenorzer et al. (2004). Note that the names of these models correspond to a set of model parameters describing the model and not to the observational spectral type naming convention. These models are subsequently convolved with a rotational broadening profile with a limb-darkening coefficient 0.6, as described by Gray (1992), to determine the value of $v_{rot} \sin i$. This results in 170 ± 30 km s^{-1}, 240 ± 25 km s^{-1} and 200 ± 40 km s^{-1} for SMC X−1, LMC X−4 and Cen X−3, respectively. The selected lines and their corresponding best model are shown in Fig. 10. The rotational velocities required for a synchronous orbit are 185 km s^{-1}, 250 km s^{-1} and 255 km s^{-1} for SMC X−1, LMC X−4 and Cen X−3, respectively. We will find below that these correspond to rotation rates consistent with, though perhaps slightly slower than, a synchronous orbit.

Since for Roche-lobe overflow systems $\beta \gtrsim 0.9$ (Avni & Bahcall 1975), we follow the approach of Rappaport & Joss (1983) and adopt that β is in the range 0.9–1.0. Thus, given a set of K_{opt}, P, $a_X \sin i$ and θ_e, we can determine by means of Monte-Carlo simulations a 1σ confidence range for the values of R_L/a, i, M_{opt} and M_X (see Rappaport & Joss 1983; Van Kerkwijk et al. 1995a).

Since in these systems soft X-rays are absorbed by the extended stellar wind of the optical companion, the eclipse lasts longer at low energies (up to ∼5 keV), depending on the density structure of the stellar wind of the optical companion (e.g. for 4U 1700−37 the eclipse at energies up to ∼2 keV lasts almost twice as long as at ∼6 keV; see Haberl et al. 1994;
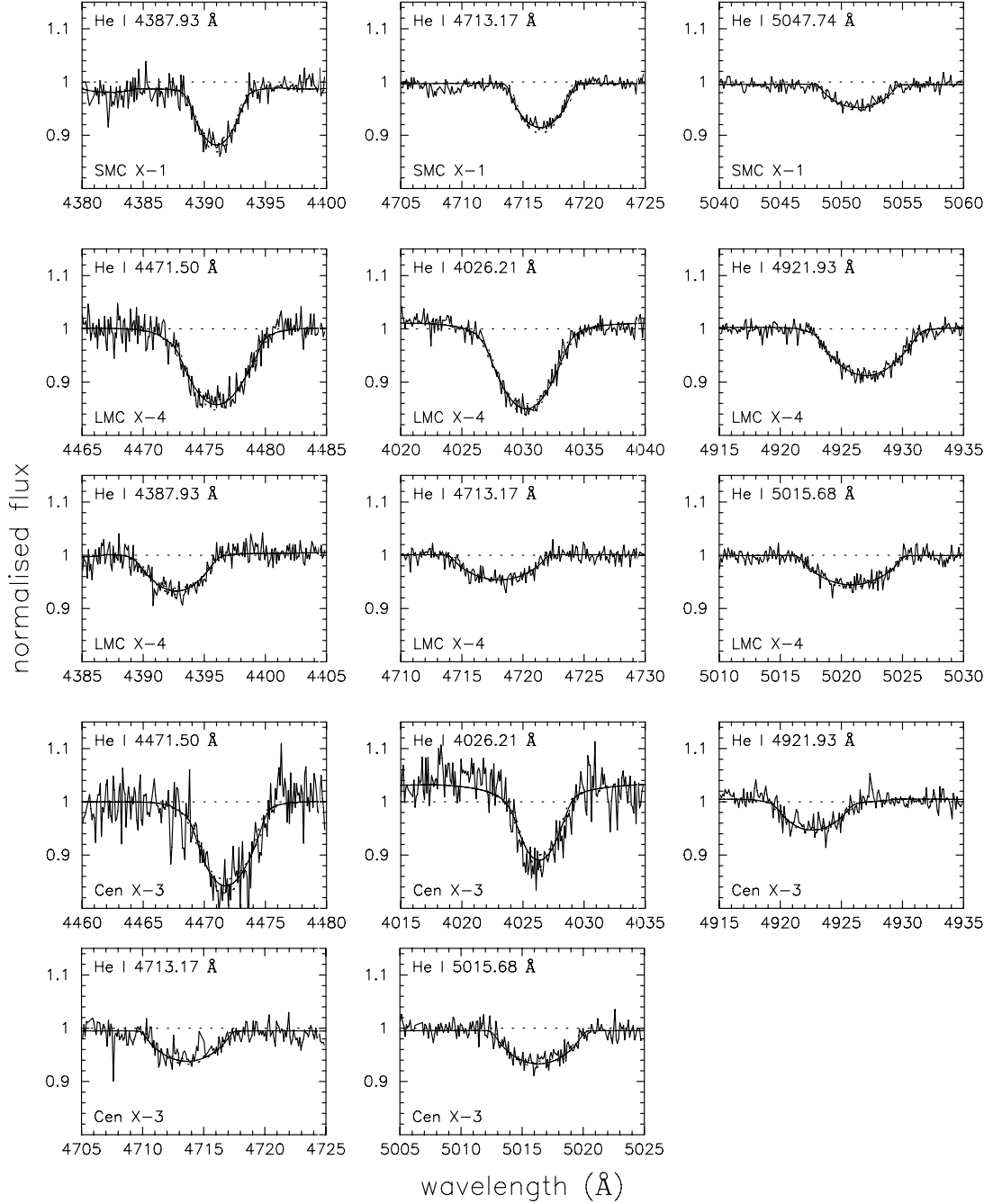
Fig. 10. Selection of lines for which we measured the rotational broadening. Each diagram includes a solid line representing the model that we applied; the dotted line represents the continuum. To better visualise the model, the spectra are smoothed with 7 resolution elements. *The top panels* show the modelled spectral lines of SMC X−1, *the second and third row* include lines of LMC X−4 and *the two bottom rows* show lines of Cen X−3.

Van der Meer et al. 2005). Therefore, we prefer θ_e determinations obtained from X-ray observations at high energies (see Table 1). For Cen X−3 these measurements are available. An accurate modelling of the X-ray light curve of multiple observations obtained with SAS-3/XTCA in the energy range 7.9–20 keV by Clark et al. (1988) results in a value of $\theta_e = 32.9° \pm 1.4°$. They do not list an error on their value, so we use the standard deviation in their θ_e distribution. For SMC X−1 and LMC X−4 no detailed modelling has been performed and θ_e measurements are mainly reported for older X-ray missions. We

use the range 26°–30.5° for SMC X−1 based on observations of Primini et al. (1976) (28.2° ± 0.9°, 2–6 keV, SAS-3), Bonnet-Bidaud & Van der Klis (1981) (29.9° ± 0.2°, 2–12 keV, COS-B) and Schreier et al. (1972a) (29.1° ± 2.8°, 2–6 keV, *Uhuru*). For LMC X−4 we adopt the range 25°–29° based on observations of Li et al. (1978) (29.0° ± 2.5°, 6–12 keV, SAS-3), White (1978) (26.2° ± 1.1°, 2–16 keV, ARIEL V) and Pietsch et al. (1985) (27.1° ± 1.0°, 2–7 keV, EXOSAT).

Using the defined input distributions for the Monte-Carlo simulations, we can determine the distributions for i, Ω, R_L/a,
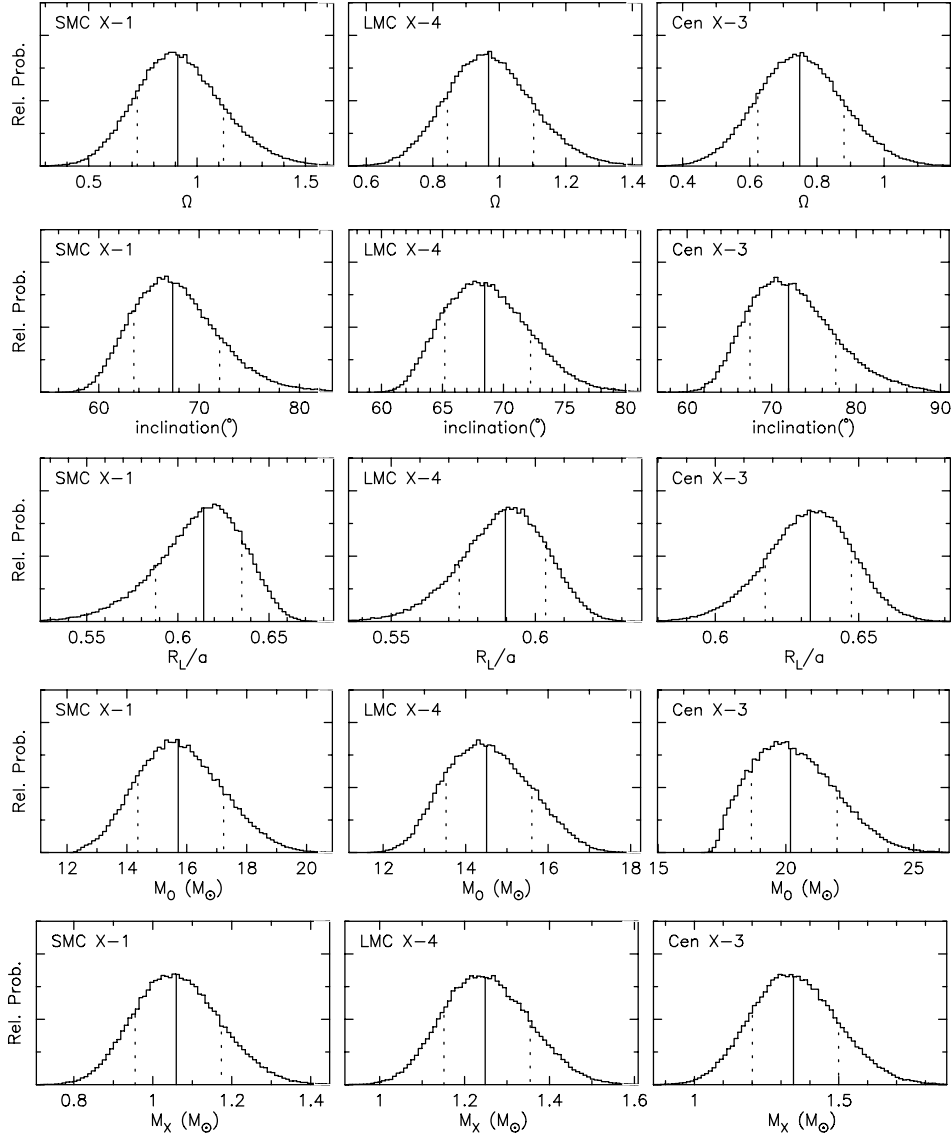
Fig. 11. Resulting probability distributions from the Monte-Carlo simulations for SMC X−1 (*left column*), LMC X−4 (*middle column*) and Cen X−3 (*rigth column*). Shown are the ratio of the rotational and orbital frequency (Ω), the inclination angle (i), the ratio of the Roche-lobe radius and the orbital separation (R_L/a) and the masses of both components (M_{opt} & M_X) of the three systems. The mean value and 1σ limits are shown with solid and dotted lines, respectively.

R_{opt}, a, M_{opt} and M_X. All the results are listed in Table 6 and some of the corresponding distributions are shown in Fig 11. The masses of the neutron stars become: $M_X = 1.06^{+0.11}_{-0.10}\ M_\odot$ for SMC X−1, $M_X = 1.25^{+0.11}_{-0.10}\ M_\odot$ for LMC X−4 and $M_X = 1.34^{+0.16}_{-0.14}\ M_\odot$ for Cen X−3 at a 1σ confidence level. Compared to the mass determinations listed in Sect. 2 the error on the neutron star mass is reduced by at least a factor two.

The masses and radii of the OB companion stars all lie in the range of 15–$20\ M_\odot$ and 8–$16\ R_\odot$, respectively, in line with previous values (Van Kerkwijk et al. 1995a). Conti (1978) and Kaper (2001) show that for these stars a higher mass is expected based on their spectral classification and conclude that these stars are undermassive for their luminosity. This may be due to the phase of mass transfer prior to the supernova forming the neutron star in the system. A detailed modelling of the optical spectra of the OB companions will be presented in a forthcoming paper.

6. The neutron star mass distribution

Abubekerov et al. (2004) present a new method to derive the radial velocity curves for HMXB systems in which the optical component is deformed due to the (partial) filling of its Roche-lobe. They show that these systems are affected by gravitational darkening and by X-ray heating of the surface of the optical component. This can result in an underestimate of the radial velocity amplitude of the optical component and therefore in an underestimate of the mass of the neutron star. Since this will mostly affect systems hosting a bright X-ray source, Roche-lobe over-flow systems will suffer most from this effect, i.e. the systems discussed in this paper. With our VLT/UVES observations it is possible for the first time to accurately determine the radial velocity amplitude of each absorption line separately. We showed that for lines that vary in EW the radial velocity is indeed underestimated by several km s^{-1}, consistent with the predictions of Abubekerov et al. (2004). By applying our carefully chosen selection criteria, we anticipate for these effects.

Table 6. List of final values for the radial velocity amplitude (K_{opt}) and the results from the output of the Monte-Carlo simulations, i.e. the values of the inclination angle (i), the ratio of the rotational and orbital frequency (Ω), the ratio of the Roche-lobe radius and the orbital separation (R_L/a), the radius of the optical companion (R_{opt}), the orbital separation (a), and the masses of both components (M_{opt} & M_X) of the three systems. All errors are 1σ.

	SMC X−1	LMC X−4	Cen X−3
K_{opt} (km s^{-1})	20.2 ± 1.1	35.1 ± 1.5	27.5 ± 2.3
i (deg)	67^{+5}_{-4}	68^{+4}_{-3}	72^{+6}_{-5}
Ω	$0.91^{+0.21}_{-0.19}$	$0.97^{+0.14}_{-0.12}$	0.75 ± 0.13
R_L/a	$0.61^{+0.02}_{-0.03}$	$0.59^{+0.01}_{-0.02}$	$0.63^{+0.01}_{-0.02}$
R_{opt} ($R_\odot$)	$16.4^{+1.0}_{-1.1}$	$7.8^{+0.3}_{-0.4}$	12.1 ± 0.5
a ($R_\odot$)	26.6 ± 0.8	13.3 ± 0.3	$19.1^{+0.6}_{-0.5}$
M_{opt} ($M_\odot$)	$15.7^{+1.5}_{-1.4}$	$14.5^{+1.1}_{-1.0}$	$20.2^{+1.8}_{-1.5}$
M_X ($M_\odot$)	$1.06^{+0.11}_{-0.10}$	$1.25^{+0.11}_{-0.10}$	$1.34^{+0.16}_{-0.14}$

We conclude that with our observations we have significantly improved the accuracy of the determination of the radial-velocity amplitude, and subsequently the determination of the neutron star mass in these three systems. Whereas some HMXB systems have shown to host a neutron star with a mass significantly higher than 1.4 $M_\odot$, as is the case for Vela X−1 and possibly 4U 1700−37, the mass of SMC X−1 is low, $1.06^{+0.11}_{-0.10}$ $M_\odot$. The masses of LMC X−4 and Cen X−3 are $1.25^{+0.11}_{-0.10}$ and $1.34^{+0.16}_{-0.14}$ $M_\odot$, respectively. The mass of SMC X−1 is just above the minimum neutron star mass of ~1 $M_\odot$ and significantly different from the mass of the neutron star in Vela X−1. We conclude that the neutron stars in HMXBs have different masses, i.e. they do not all have the same "canonical" mass. We illustrate our new mass derivations in Fig. 12, as part of the neutron star masses reported by Stairs (2004) and references therein for neutron stars in different types of systems.

7. Discussion

It remains to be explained why the mass of SMC X−1 is well below 1.28 $M_\odot$. The low mass may be the result of a different formation scenario, i.e. the electron-capture collapse of a degenerate O-Ne-Mg core. Van den Heuvel (2004) argues that the generally low masses of neutron stars measured in binary radio pulsar systems may be due to a selection effect, as follows. Pfahl et al. (2002) noticed that there are two classes among the wide Be/X-ray binaries: (1) a substantial group with low orbital eccentricities, which indicates that their neutron stars received hardly any velocity kick in their formation events, and (2) a group with high orbital eccentricities, in which the neutron stars must have received a kick velocity of several hundreds of km s^{-1} in their birth events.

It was subsequently noticed (Van den Heuvel 2004) that the low orbital eccentricities of 5 out of the 7 known double neutron stars in the galactic disc indicate that the second-born neutron stars in these systems received hardly any kick velocity during their birth events and thus appear to belong to the same low-kick class of neutron stars as the ones in the low-eccentricity Be/X-ray binaries. These second-born neutron stars in the low-eccentricity double neutron star systems all appear to have low masses, in the range 1.18−1.36 $M_\odot$. This fits excellently with neutron-star formation by the electron-capture collapse of a degenerate O-Ne-Mg core, which is expected to form at the end of the evolution of stars that originated in the main-sequence mass-range 8 to about 13 ± 1 $M_\odot$ (Miyaji et al. 1980; Podsiadlowski

et al. 2005; Kitaura et al. 2005). Stars with larger masses develop at the end of their lives a collapsing iron core, surrounded by convective shells with O - and Si -burning. The violent convection in these shells may create large density inhomogeneities in the layers surrounding the proto-neutron-star formed by the collapsing iron core. This may lead to large anisotropies in the neutrino transport through these layers, which may cause the neutron star to be imparted with a "kick" velocity of some 500 km s^{-1} (Burrows & Hayes 1996; Scheck et al. 2004). Indeed, young single radio pulsars have large space velocities (Gunn & Ostriker 1970) and their velocity distribution is very well represented by a Maxwellian with a characteristic mean velocity of about 400 km s^{-1} (Hobbs et al. 2005).

In the light of these findings the low mass of the neutron star in SMC X−1 would be consistent with its formation by electron-capture collapse in a degenerate O-Ne-Mg core. This would imply a main-sequence progenitor mass ≲14 $M_\odot$. Presently the companion of SMC X−1 has a mass of about 16 $M_\odot$. Allowing for some mass loss by stellar wind, its mass just after the mass transfer and the formation of the neutron star would have been about 18 $M_\odot$.

With an explosive mass loss during the formation of the neutron star of about 1 $M_\odot$ and a few solar masses stellar wind mass loss from the neutron-star progenitor, the initial system must have had a mass ≳22 $M_\odot$ (including the neutron-star mass). Thus, a progenitor system of 13 $M_\odot$+9 $M_\odot$ (or 14 $M_\odot$ + 8 $M_\odot$) would be consistent with the present system configuration. A potential problem with such a configuration is that conservation of mass and orbital angular momentum during mass transfer would lead to a fairly wide presupernova system, such that the present orbital period of ~3.9 days would be hard to understand, unless a large amount of orbital angular momentum has been lost with relatively little mass (at most a few solar masses) from the system. We thus conclude that the low mass of the neutron star in SMC X−1 is consistent with formation by electron-capture collapse, provided that a relatively large amount of orbital angular momentum was lost from the system during the first phase of mass transfer.
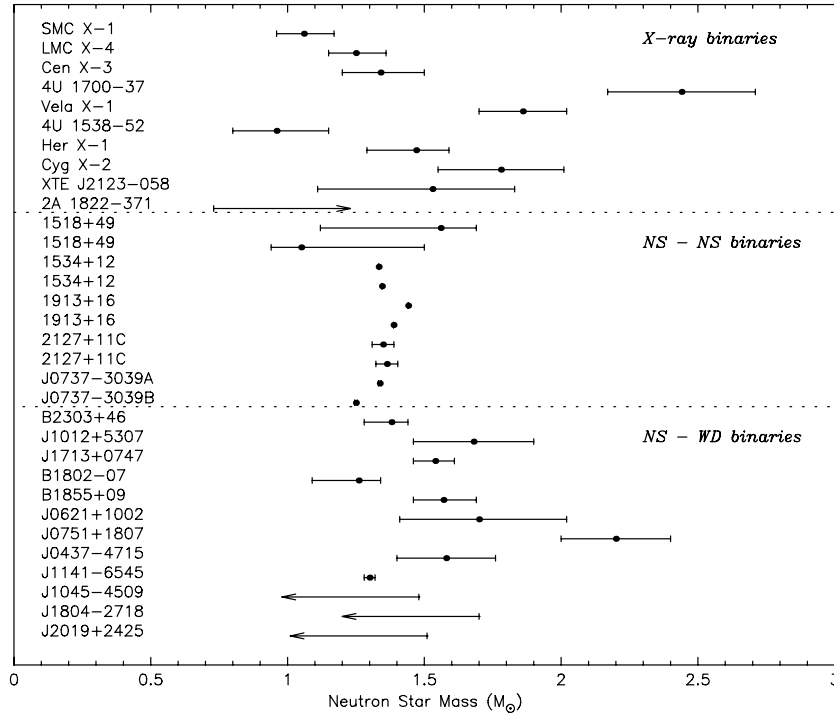
Fig. 12. Neutron Star (NS) masses in X-ray binaries, NS−NS binaries and NS−White Dwarf (WD) binaries obtained from Stairs (2004) and references therein. The indicated masses of SMC X−1, LMC X−4 and Cen X−3 are obtained from this study. The error bars correspond to 1σ errors. This plot clearly suggests that neutron stars do not all have the same "canonical" mass. Note that although 4U 1700−37 most probably is a neutron star, it could be a black hole.

References

Abubekerov, M. K., Antokhina, E. A., & Cherepashchuk, A. M. 2004, Astron. Rep., 48, 89

Ash, T. D. C., Reynolds, A. P., Roche, P., et al. 1999, MNRAS, 307, 357

Aslanov, A. A., & Cherepashchuk, A. M. 1982, AZh, 59, 290

Avni, Y., & Bahcall, J. N. 1975, ApJ, 197, 675

Barziv, O., Kaper, L., Van Kerkwijk, M. H., Telting, J. H., & Van Paradijs, J. 2001, A&A, 377, 925

Bildsten, L., Chakrabarty, D., Chiu, J., et al. 1997, ApJS, 113, 367

Blondin, J. M. 1994, ApJ, 435, 756

Bonnet-Bidaud, J. M. & Van der Klis, M. 1981, A&A, 97, 134

Brown, G. E. & Bethe, H. A. 1994, ApJ, 423, 659

Burrows, A. 2000, Nature, 403, 727

Burrows, A. & Hayes, J. 1996, Phys. Rev. Lett., 76, 352

Chevalier, C. & Ilovaisky, S. A. 1977, A&A, 59, L9

Chodil, G., Mark, H., Rodrigues, R., et al. 1967, Phys. Rev. Lett., 19, 681

Clark, G. W., Minato, J. R., & Mi, G. 1988, ApJ, 324, 974

Clarkson, W. I., Charles, P. A., Coe, M. J., et al. 2003, MNRAS, 339, 447

Conti, P. S. 1978, A&A, 63, 225

Conti, P. S., & Alschuler, W. R. 1971, ApJ, 170, 325

Crampton, D., Hutchings, J. B., & Cowley, A. P. 1985, ApJ, 299, 839

Dekker, H., D'Odorico, S., Kaufer, A., Delabre, B., & Kotzlowski, H. 2000, in Optical and IR Telescope Instrumentation and Detectors, ed. M. Iye; A. F. Moorwood; Proc. SPIE, 4008, 534

Fullerton, A. W., Gies, D. R., & Bolton, C. T. 1996, ApJS, 103, 475

Giacconi, R., Gursky, H., Kellogg, E., Schreier, E., & Tananbaum, H. 1971, ApJ, 167, L67+

Giacconi, R., Murray, S., Gursky, H., et al. 1972, ApJ, 178, 281

Gies, D. R., Bagnuolo, W. G., & Penny, L. R. 1997, ApJ, 479, 408

Gray, D. F. 1992, The Observation and Analysis of Stellar Photospheres, The Observation and Analysis of Stellar Photospheres, ed. by D. F. Gray (Cambridge, UK: Cambridge University Press), 470

Gunn, J. E., & Ostriker, J. P. 1970, ApJ, 160, 979

Haberl, F., Aoki, T., & Mavromatakis, F. 1994, A&A, 288, 796

Haensel, P., Zdunik, J. L., & Douchin, F. 2002, A&A, 385, 301

Heemskerk, M. H. M., & Van Paradijs, J. 1989, A&A, 223, 154

Hilditch, R. W., Howarth, I. D., & Harries, T. J. 2005, MNRAS, 357, 304

Hillier, D. J., & Miller, D. L. 1998, ApJ, 496, 407

Hiltner, W. A., Werner, J., & Osmer, P. 1972, ApJ, 175, L19

Hobbs, G., Lorimer, D. R., Lyne, A. G., & Kramer, M. 2005, MNRAS, 360, 974

Hut, P. 1981, A&A, 99, 126

Hutchings, J. B., Crampton, D., & Cowley, A. P. 1978, ApJ, 225, 548

Hutchings, J. B., Cowley, A. P., Crampton, D., Van Paradus, J., & White, N. E. 1979, ApJ, 229, 1079

Jacoby, B. A., Hotan, A., Bailes, M., Ord, S., & Kulkarni, S. R. 2005, ApJ, 629, L113

Jones, C., Forman, W., Tananbaum, H., et al. 1973, ApJ, 181, L43

Joss, P. C., & Rappaport, S. A. 1984, ARA&A, 22, 537

Kaper, L. 2001, in The Influence of Binaries on Stellar Population Studies, ASSL, 264, 125

Kaper, L., & Van der Meer, A. 2005, ArXiv Astrophysics e-prints

Kaper, L., Hammerschlag-Hensberge, G., & Zuiderwijk, E. J. 1994, A&A, 289, 846

Kelley, R. L., Jernigan, J. G., Levine, A., Petro, L. D., & Rappaport, S. 1983, ApJ, 264, 568

Kitaura, F. S., Janka, H., & Hillebrandt, W. 2005, ArXiv Astrophysics e-prints

Krzeminski, W. 1974, ApJ, 192, L135

Lang, F. L., Levine, A. M., Bautz, M., et al. 1981, ApJ, 246, L21

Lattimer, J. M., & Prakash, M. 2004, Science, 304, 536

Lennon, D. J., Dufton, P. L., & Fitzsimmons, A. 1993, A&AS, 97, 559

Lenorzer, A., Mokiem, M. R., de Koter, A., & Puls, J. 2004, A&A, 422, 275

Levine, A., Rappaport, S., Deeter, J. E., Boynton, P. E., & Nagase, F. 1993, ApJ, 410, 328

Levine, A. M., Rappaport, S. A., & Zojcheski, G. 2000, ApJ, 541, 194

Li, F., Rappaport, S., & Epstein, A. 1978, Nature, 271, 37

Liller, W. 1973, ApJ, 184, L37

Lutovinov, A., Revnivtsev, M., Gilfanov, M., et al. 2005, A&A, 444, 821

Mason, K. O., Branduardi, G., & Sanford, P. 1976, ApJ, 203, L29

Miyaji, S., Nomoto, K., Yokoi, K., & Sugimoto, D. 1980, PASJ, 32, 303

Mokiem, M. R., de Koter, A., Puls, J., et al. 2005, A&A, 441, 711

Nagase, F., Corbet, R. H. D., Day, C. S. R., et al. 1992, ApJ, 396, 147

Negueruela, I., Smith, D. M., Reig, P., Chaty, S., & Torrejón, J. M. 2006, in ESA Special Publication, ed. A. Wilson, 604, 165

Nice, D., Splaver, E., Stairs, I., et al. 2005, ArXiv Astrophysics e-prints

Paul, B., Raichur, H., & Mukherjee, U. 2005, ArXiv Astrophysics e-prints

Petro, L. D., & Hiltner, W. A. 1982, NASA STI/Recon Technical Report N, 85, 19905

Pfahl, E., Rappaport, S., Podsiadlowski, P., & Spruit, H. 2002, ApJ, 574, 364

Pietsch, W., Voges, W., Pakull, M., & Staubert, R. 1985, Space Sci. Rev., 40, 371

Podsiadlowski, P., Dewi, J. D. M., Lesaffre, P., et al. 2005, MNRAS, 361, 1243

Priedhorsky, W. C., & Terrell, J. 1983, ApJ, 273, 709

Primini, F., Clark, G. W., Lewin, W., et al. 1976, ApJ, 210, L71

Quaintrell, H., Norton, A. J., Ash, T. D. C., et al. 2003, A&A, 401, 313

Rappaport, S. A., & Joss, P. C. 1983, in Accretion-Driven Stellar X-ray Sources, 1

Reynolds, A. P., Bell, S. A., & Hilditch, R. W. 1992, MNRAS, 256, 631

Reynolds, A. P., Hilditch, R. W., Bell, S. A., & Hill, G. 1993, MNRAS, 261, 337

Reynolds, A. P., Owens, A., Kaper, L., Parmar, A. N., & Segreto, A. 1999, A&A, 349, 873

Sahade, J. 1959, PASP, 71, 151

Sahade, J. 1962, in Proceedings of a Symposium on Stellar Evolution, held in La Plata, November 7–11, 1960, La Plata: National University, Astronomical Observatory, ed. J. Sahade, 185

Sanduleak, N., & Philip, A. G. D. 1976, IAU Circ., 3023, 1

Savonije, G. J. 1978, A&A, 62, 317

Savonije, J. 1983, in Accretion-Driven Stellar X-ray Sources, 343

Scheck, L., Plewa, T., Janka, H.-T., Kifonidis, K., & Müller, E. 2004, Phys. Rev. Lett., 92, 011103

Schreier, E., Giacconi, R., Gursky, H., Kellogg, E., & Tananbaum, H. 1972a, ApJ, 178, L71

Schreier, E., Levinson, R., Gursky, H., et al. 1972b, ApJ, 172, L79

Schrijvers, C., & Telting, J. H. 1999, A&A, 342, 453

Schrijvers, C., Telting, J. H., Aerts, C., Ruymaekers, E., & Henrichs, H. F. 1997, A&AS, 121, 343

Srinivasan, G. 2001, in Black Holes in Binaries and Galactic Nuclei, 45

Stairs, I. H. 2004, Science, 304, 547

Struve, O. 1937, ApJ, 85, 41

Thorsett, S. E., & Chakrabarty, D. 1999, ApJ, 512, 288

Timmes, F. X., Woosley, S. E., & Weaver, T. A. 1996, ApJ, 457, 834

Tjemkes, S. A., Van Paradijs, J., & Zuiderwijk, E. J. 1986, A&A, 154, 77

Val Baker, A. K. F., Norton, A. J., & Quaintrell, H. 2005, A&A, 441, 685

Van den Heuvel, E. P. J. 2004, in 5th INTEGRAL Workshop on the INTEGRAL Universe, ESA SP-552, 185

Van der Meer, A., Kaper, L., di Salvo, T., et al. 2005, A&A, 432, 999

Van Kerkwijk, M. H., Van Paradijs, J., & Zuiderwijk, E. J. 1995a, A&A, 303, 497

Van Kerkwijk, M. H., Van Paradijs, J., Zuiderwijk, E. J., et al. 1995b, A&A, 303, 483

Van Paradijs, J. A., Hammerschlag-Hensberge, G., & Zuiderwijk, E. J. 1978, A&AS, 31, 189

Vidal, N. V., Wickramsinghe, D. T., & Peterson, B. A. 1973, ApJ, 182, L77

White, N. E. 1978, Nature, 271, 38

Wojdowski, P., Clark, G. W., Levine, A. M., Woo, J. W., & Zhang, S. N. 1998, ApJ, 502, 253

Online Material

Table 2. Observing log of the three observed systems. For each observation the Modified Julian Date (MJD) corresponding to the mid-exposure time is given, the orbital phase (ϕ) and the signal-to-noise ratio (S/N) per resolution element of the three different CCDs centered at 4270 Å for the blue CCD, 5150 Å for the red1 CCD and 6100 Å for the red2 CCD.

MJD (days)	SMC X−1 orbital phase(ϕ)	S/N blue	red1	red2	MJD (days)	LMC X−4 orbital phase(ϕ)	S/N blue	red1	red2	MJD (days)	Cen X−3 orbital phase(ϕ)	S/N blue	red1	red2
52 187.154	0.537	58	75	69	52 214.187	0.388	54	69	58	52 271.300	0.462	33	67	77
52 214.090	0.458	60	80	71	52 224.249	0.533	43	58	50	52 287.229	0.095	22	50	64
52 224.224	0.062	49	69	62	52 225.255	0.247	49	66	57	52 292.273	0.512	27	57	68
52 225.211	0.315	58	78	68	52 226.212	0.927	48	67	56	52 298.169	0.337	32	63	75
52 242.059	0.644	41	61	54	52 237.314	0.809	54	72	63	52 309.323	0.681	35	76	81
52 243.087	0.908	66	77	70	52 242.282	0.337	55	71	61	52 313.150	0.515	37	74	78
52 244.168	0.186	67	81	74	52 243.113	0.927	54	62	55	52 321.163	0.354	29	64	72
52 247.185	0.961	43	58	51	52 244.193	0.694	59	67	55	52 322.158	0.831	31	65	73
52 256.112	0.255	53	66	59	52 245.213	0.418	67	73	65	52 326.186	0.761	38	77	82
52 258.094	0.764	58	69	62	52 246.085	0.037	44	53	45	52 327.277	0.284	37	77	85
52 270.052	0.837	61	74	68	52 256.086	0.138	32	40	35	52 328.241	0.746	41	82	88
52 271.059	0.095	52	65	60	52 259.094	0.274	49	59	50	52 329.260	0.234	38	76	86
52 285.112	0.706	47	61	56	52 261.163	0.743	58	71	61					

Table 5. Weighted mean values of the radial velocity for each spectrum, indicated by its orbital phase (ϕ) for SMC X−1, LMC X−4, and Cen X−3. All errors are 1σ.

| SMC X−1 ϕ	$\langle v_{\rm rad}\rangle$ (km s^{-1})	LMC X−4 ϕ	$\langle v_{\rm rad}\rangle$ (km s^{-1})	Cen X−3 ϕ	$\langle v_{\rm rad}\rangle$ (km s^{-1})
0.062	8.42 ± 1.06	0.037	6.45 ± 1.50	0.095	14.96 ± 2.97
0.096	19.04 ± 1.02	0.138	29.28 ± 2.23	0.234	22.87 ± 2.10
0.186	16.58 ± 0.77	0.247	40.06 ± 1.38	0.284	31.47 ± 1.98
0.255	24.42 ± 1.17	0.274	30.03 ± 1.60	0.337	14.12 ± 2.59
0.315	14.70 ± 0.95	0.337	24.84 ± 1.24	0.354	18.43 ± 2.75
0.458	4.98 ± 0.84	0.388	25.04 ± 1.33	0.462	−10.75 ± 2.86
0.537	−9.37 ± 1.01	0.418	23.23 ± 1.10	0.512	−21.61 ± 2.42
0.645	−18.46 ± 1.24	0.533	−14.69 ± 1.54	0.681	−26.12 ± 2.19
0.707	−19.07 ± 1.08	0.694	−30.90 ± 1.21	0.746	−18.81 ± 1.76
0.765	−16.47 ± 0.89	0.743	−34.06 ± 1.17	0.761	−23.29 ± 2.07
0.837	−19.83 ± 0.87	0.809	−30.86 ± 1.16	0.831	−24.32 ± 2.34
0.909	−8.22 ± 0.77	0.927	−17.96 ± 1.19	0.515	−14.55 ± 1.98
0.961	−1.85 ± 1.09	0.927	−17.95 ± 1.12		
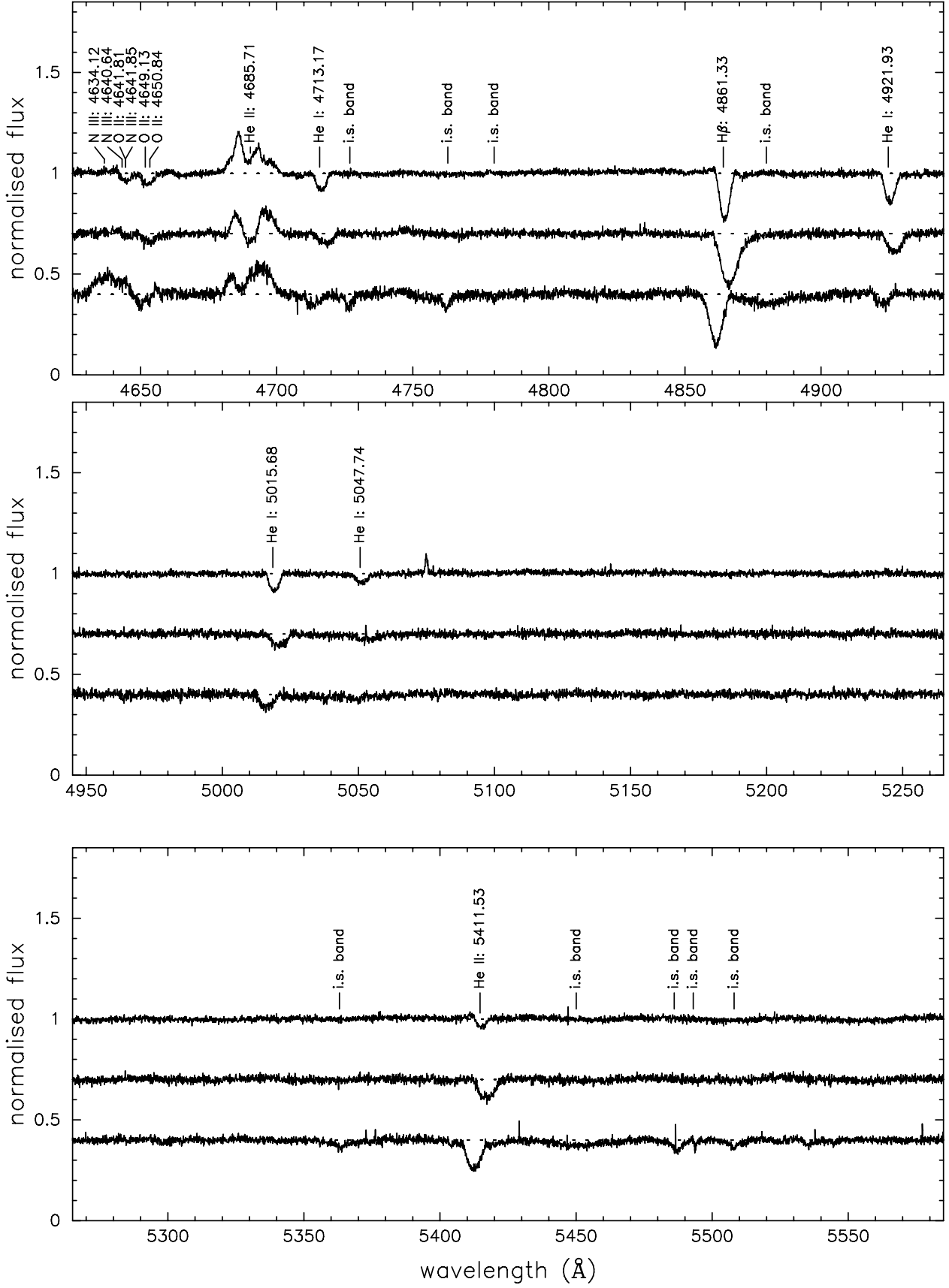
Fig. 2. Normalised spectra in the wavelength range 4625–5585 Å of SMC X−1 at orbital phase ϕ = 0.06 (*top spectrum*), LMC X−4 at orbital phase ϕ = 0.04 (*middle spectrum*) and Cen X−3 at orbital phase ϕ = 0.09 (*bottom spectrum*), respectively. The line identifications are shown above the spectrum of SMC X−1.
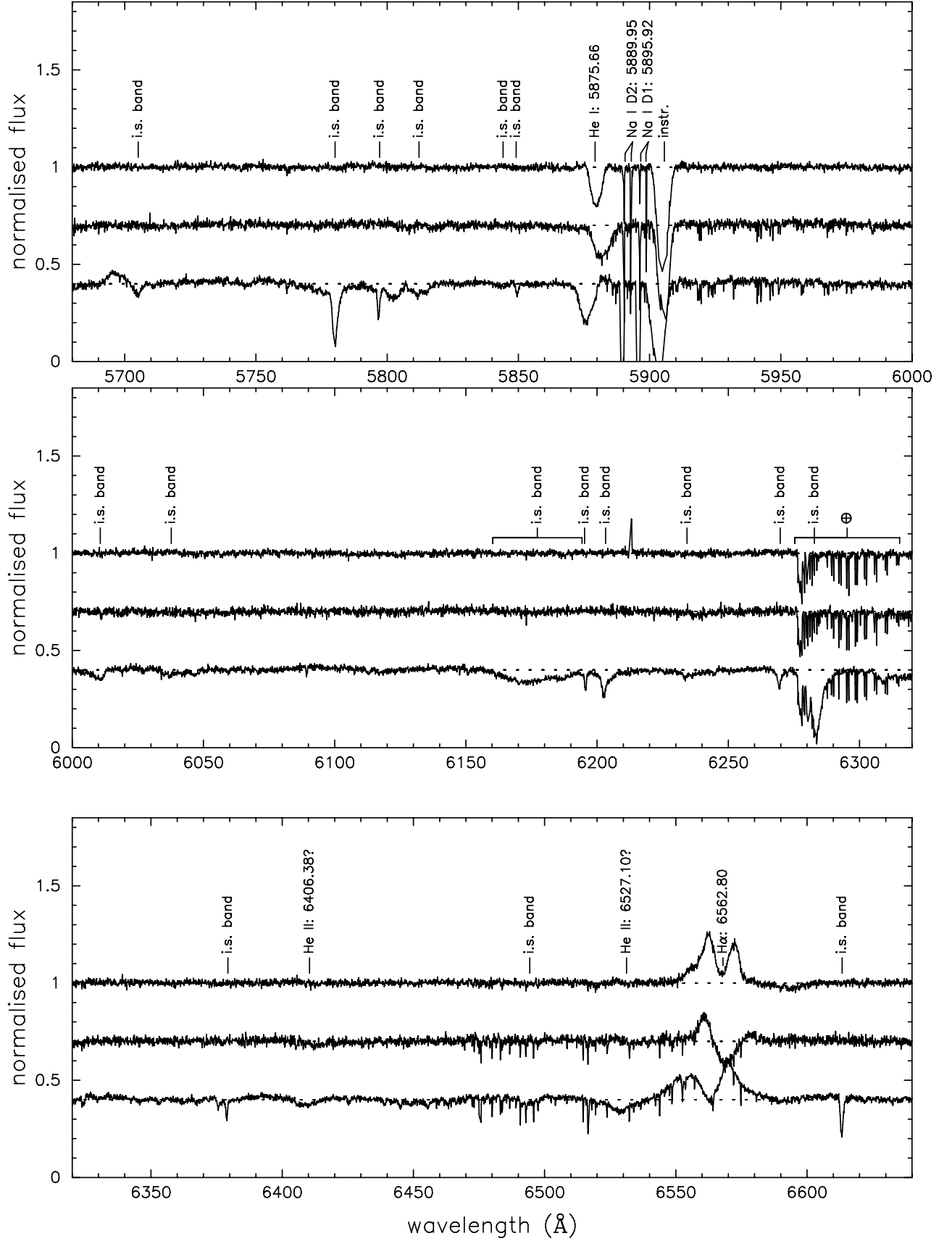
Fig. 3. Normalised spectra in the wavelength range 5680–6640 Å of SMC X−1 at orbital phase ϕ = 0.06 (*top spectrum*), LMC X−4 at orbital phase ϕ = 0.04 (*middle spectrum*) and Cen X−3 at orbital phase ϕ = 0.09 (*bottom spectrum*), respectively. The line identifications are shown above the spectrum of SMC X−1.